Monthly Notices of the ROYAL ASTRONOMICAL SOCIETY
MNRAS **451,** 3693–3708 (2015) doi:10.1093/mnras/stv1102

Galactic chemical evolution: stellar yields and the initial mass function

Mercedes Mollá,[1,2★] Oscar Cavichia,[2,3★] Marta Gavilán[4] and Brad K. Gibson[5]

[1]*Departamento de Investigación Básica, CIEMAT, Avda. Complutense 40, E-28040 Madrid, Spain*
[2]*IAG, Universidade de São Paulo, Rua do Matão, 1226, 05508-090 São Paulo-SP, Brazil*
[3]*Departamento de Física, Universidade Federal de Itajubá, Av. BPS, 1303, 37500-903 Itajubá-MG, Brazil*
[4]*Departamento de Física Teórica, Universidad Autónoma de Madrid, Cantoblanco, E-28049, Madrid, Spain*
[5]*E.A. Milne Centre for Astrophysics, Department of Physics & Mathematics, University of Hull, Hull HU6 7RX, UK*

Accepted 2015 May 13. Received 2015 May 12; in original form 2015 November 28

ABSTRACT

We present a set of 144 Galactic chemical evolution models applied to a Milky Way analogue, computed using four sets of low+intermediate star nucleosynthetic yields, six massive star yield compilations, and six functional forms for the initial mass function. A comparison is made between a grid of multiphase chemical evolution models computed with these yield combinations and empirical data drawn from the Milky Way's disc, including the solar neighbourhood. By means of a χ^2 methodology, applied to the results of these multiphase models, the best combination of stellar yields and initial mass function capable of reproducing these observations is identified.

Key words: stars: abundances – stars: mass-loss – Galaxy: abundances – Galaxy: disc – Galaxy: evolution.

1 INTRODUCTION

Chemical evolution models (CEMs) were developed initially to understand observations such as the local metallicity distribution of G/K-dwarfs and the radial gradient of abundances through the disc of late-type spirals, including the Milky Way Galaxy (MWG). The basic framework for a CEM involves a volume of a galaxy within which gas is assumed to flow, both inwards via infall and radial flows, as well as outflows; an adopted star formation prescription, coupled with an initial mass function (IMF), then allows the calculation of the production rate of stars of a given mass, supernovae, and the ejection rate of nucleosynthetic products back to the interstellar medium (ISM). The latter is often characterized via the use of *stellar yields* and the integrated or *true* yields, concepts first introduced by Tinsley (1980). While the infall and star formation rates (SFRs) are essential to create and maintain a certain radial abundance gradient, the IMF and the stellar yields define the absolute level observed in a region. It is therefore critical to understand the origin of the elements and, in particular, the specific stars from which individual chemical elements originate, the quantity returned by each said star, and the time-scale for their ejection back into the ISM.

Since the seminal work of Burbidge et al. (1957) much has been done to improve our understanding of stellar nucleosynthesis. Early work focused on stars with metallicities similar to that of the Sun, with contemporary work now concerned with spanning the full range of metallicities encountered in nature. However, code-to-code differences still result in substantive differences in the predicted stellar yields across these mass ranges (e.g. Gibson, Loewenstein & Mushotzky 1997). Due to the quite different end-lives of massive stars, as opposed to low + intermediate-mass stars, stellar evolution codes have typically separated their applicability to either those which end their lives as Type II supernovae (SN-II) or those which end their lives as white dwarfs.

For massive stars, the total yields of elements are usually provided for those originating from the supernova explosions or those originating from pre-explosion stellar winds; only rarely are both provided, self-consistently. The most frequently used set of massive stellar yields (hereafter *mas*) has been that of Woosley & Weaver (1995, hereafter WOW); to the elements produced in SN-II (for metallicities spanning $Z = 0$ to $Z_{\odot}$), WOW added the pre-supernova yields of Woosley & Weaver (1986), but did not include the contribution from pre-SN-II stellar winds. Later, Portinari, Chiosi & Bressan (1998, hereafter PCB) provided massive star yields for a range of metallicities, but now taking into account both the pre- and post-explosion elemental return rates, including the stellar winds and the subsequent effect of this mass-loss on the evolution of the star and on the ejection of the supernova explosion. More recently, Limongi & Chieffi (2003) and Chieffi & Limongi (2004, hereafter both sets referred to as CLI), Limongi & Chieffi (2006) and Limongi & Chieffi (2012, hereafter both sets referred to as LIM), Kobayashi et al. (2006, hereafter KOB) and Rauscher et al. (2002); Fröhlich et al. (2006), and Heger & Woosley (2010, hereafter the joined sets referred to as HEG) have calculated new massive stars yields.[1] We will use all these sets in this work.

★E-mail: mercedes.molla@ciemat.es (MM); cavichia@unifei.edu.br (OC)

[1] Chieffi & Limongi (2013) also give new stellar yields but only for solar metallicity stars and for this reason they are not used here.

For the low and intermediate mass star (hereafter *lim*) yields, besides the seminal work of Renzini & Voli (1981), where the effects of convective dredge-up and the so-called Hot Bottom Burning (HBB) processes were taken into account, more recent yield compilations have been provided by Forestini & Charbonnel (1997), Ventura & D'Antona (2005), van den Hoek & Groenewegen (1997, hereafter VHK), Marigo (2001, hereafter MAR), Gavilán, Buell & Mollá (2005), Gavilán, Mollá & Buell (2006, both hereafter GAV), and Karakas (2010, hereafter KAR). A consequence of an ever-improving knowledge of asymptotic giant branch (AGB) physics, is the reduction in the differences in the published yields, in particular for the CNO elements. Thus, the work done by Stancliffe & Jeffery (2007), centred on the mass-loss rates, shows that changes in the yield by up to ∼80 per cent can result, but only for certain isotopes. On the other hand, Ventura & D'Antona (2009) focus their efforts on calculating new yields with significantly improved values of the opacity. Finally, Campbell & Lattanzio (2008) and Gil-Pons et al. (2013) devote their work to the case of extremely metal poor stars, whose final evolutionary characteristics are not well known at the present. Apart from the AGB evolution, other authors have emphasized the importance of the nuclear reactions and their associated numerical parameters; this is the case for KAR and also Cristallo et al. (2009). The former rederived the yields of Karakas & Lattanzio (2007) with new values of proton capture. The main differences with previous works reside in the yields of ^{19}F, ^{23}Na and neutron rich isotopes.[2] Nevertheless, the CNO yields do not change significantly amongst these works.

Other important sets of yields available in the literature, such as Siess (2010), have not been incorporated into our analysis. These authors provide yields for super-AGB stars with masses in the range 7.5–10.5 $M_\odot$ and metallicities between $Z = 1e{-}4$ and 0.04. The use of these tables implies a change in the mass at which one star explodes as an SN-II, $m_{\text{SN-II}}$, and, more importantly, it introduces a third stellar mass range, instead of the two currently used (for low+intermediate and high-mass stars). We prefer for simplicity to adopt a constant, metallicity-independent, value of $m_{\text{SN-II}} = 8\,M_\odot$, rather than introduce an additional free parameter. We will explore the influence of this sort of metallicity-dependent SN-II mass limit, coupled with extant super-AGB yields, in the next future.

Concerning the IMF, it is still matter of discussion if it is constant for all type of galaxies or if there are differences with environment, dependences upon Galactic stellar mass or metallicity, or on the local SFR. Many recent works suggest that the IMF depends on the SFR and/or metallicity of the regions (e.g. Bekki 2013; Conroy et al. 2013; Dopcke et al. 2013; Ferreras et al. 2013; Geha et al. 2013; Läsker et al. 2013; McWilliam, Wallerstein & Mottini 2013; Smith & Lucey 2013; Weidner et al. 2013, and references therein), implying in most cases that the IMF might also be variable with time, but with disagreement among their results. Calura et al. (2010) used in a CEM an IMF which depends on the embedded cluster mass function, resulting in an IMF variable with time, as a function of the SFR. They conclude that the best fit to the solar neighbourhood data occurs with an IMF resembling the standard one. Andrews et al. (2013) and Peacock et al. (2014) also support an invariant IMF for all types of systems. Regardless of these issues of invariance, the classical functional forms for the IMF employed in the literature, including those of Salpeter (1955), Miller & Scalo (1979), Ferrini, Penco & Palla (1990), Kroupa (2002), Chabrier (2003) and Maschberger (2013, hereafter SAL, MIL, FER, KRO, CHA, and MAS, respectively), whilst broadly similar, are quantitatively different from each other. In this work we will use these six forms, under the assumption that they are invariant with time.

There are numerous CEMs in the literature, with important differences in their results, even for the case of the MWG for which the observational data sets are numerous. In these works, the selection of the best model, and the corresponding free parameters, such as the SFR efficiency and/or infall rate, is performed, for any galaxy, comparing their observational data with a CEM built using a set of stellar yields with a given IMF (Gibson 1997; Gavilán, Buell & Mollá 2005; Romano et al. 2010; Carigi & Peimbert 2011). Then, if observations cannot be well-reproduced, it can be claimed that an alternate set of yields *or* IMF might be necessary (Hernández-Martínez et al. 2011). Alternatively, it is possible to compare data with models computed using different IMFs to see which of these functions are valid, without changing the stellar yields; Romano et al. (2005) did just that, concluding that Kroupa (2001), CHA, and MIL are better at reproducing the empirical data, than SAL, or Scalo (1998); Vincenzo et al. (2015) analyse the integrated yields comparing results from different IMFs. However, the abundances within a galaxy or region therein, with a given star formation history, may be very different if another *combination* of IMF + stellar yields were to be used. Both ingredients are equally important to define the elemental abundances in a region and the corresponding temporal evolution.

In this work, we make use of the multiphase CEM, originally applied in Ferrini et al. (1992, 1994) and Mollá, Ferrini & Diaz (1996) to the solar region, the Galactic disc, and to other external spiral discs, respectively. In Mollá & Díaz (2005, hereafter MD05), a large grid of models for a set of 440 theoretical galaxies was generated. In that work the IMF was taken from FER and the stellar yields were from WOW and GAV. In addition, the yields from Type Ia supernovae (SN-Ia; Iwamoto et al. 1999) were included along with the SN-Ia rate time distribution given by Ruiz-Lapuente et al. (2000). In Cavichia et al. (2014), we also used a similar model to that of MD05, applied to the MWG, modified to include bar-driven gas inflows, which has the effect of changing the SFR radial profile without significantly modifying the elemental abundance pattern.

Our objective in this new work is to compute CEMs for the MWG, with the same framework, total mass, molecular cloud and star formation efficiencies, and infall prescriptions for all of them, but with different combinations of stellar yields for massive stars (six sets), low + intermediate mass stars (four sets), and IMFs (six functions), thus resulting in a final grid of 144 models. Our aim is to identify which is the best combination able to reproduce simultaneously the greatest number of observational constraints, mainly those pertaining to the radial distributions of gas, stars, and elemental abundances, and to the evolution of the solar region.

The stellar yields and IMFs employed in our analysis are outlined in Section 2. The CEM is presented in Section 3, along with the results of the 144 models. The selection of the best models is in Section 4, making use of a χ^2 approach, after comparison with the observational data (which are provided in Appendix A). Section 5 is devoted to our conclusions.

[2] The problems of ^{19}F and ^{23}Na overproduction for AGB yields are outlined in Renda et al. (2004) and Fenner et al. (2006), respectively.

2 INGREDIENTS: STELLAR YIELDS AND IMF

2.1 Stellar yield sets

The stellar yield $q_i(m)$ is defined as the fraction of the initial mass m of a star ejected in the form of freshly synthesized element i (Pagel 2009)

$$q_i(m) = \frac{m_{\mathrm{eje,new},i}}{m} \tag{1}$$

and is related to the total mass of this element i, $m_{\mathrm{eje},\,i}(m)$, ejected by the star throughout its evolution (including pre-SN stellar winds) and death, via

$$m_{\mathrm{eje},i}(m) = m\, q_i(m) + (m - m_{\mathrm{rem}})\, X_{i,0}, \tag{2}$$

where m_{rem} is the mass of the stellar remnant and $X_{i,\,0}$ is the abundance of the element i initially present in the star.

Stellar yields are calculated by the stellar evolution community by coupling the evolution of the interior stellar structure with the relevant associated nuclear reactions. Such calculations provide the mass of each element produced and ejected to the ISM by stars of different masses throughout their lifetime. In CEMs, the stellar yields are usually divided into two ranges of stellar masses: (1) low and intermediate mass stars, which include those stars with masses $m \le 8\ \mathrm{M}_\odot$; and (2) massive stars, with $m > 8\ \mathrm{M}_\odot$, assuming that this is the minimum mass for stars which end their lives as SN-II.

2.1.1 *Low and intermediate mass stellar yields*

The main contribution from low and intermediate mass stars to the chemical enrichment is done during the AGB phase, where the mass-loss, thermal pulses, Third Dredge Up (TDU) events, and HBB are taking place. The first metallicity-dependent yields used in CEM were those from Renzini & Voli (1981). In retrospect, the low mass-loss rate adopted by the authors led to the need for a very large number of thermal pulses, to ensure reasonable remnant masses; the consequence of spending such a long time in the AGB phase was that almost of the ^{12}C was transformed into ^{14}N.

As our knowledge of stellar evolution improved, newer yields were released with more accurate mass-loss prescriptions, TDU events, and HBB. This is the case for the compilation of VHK, whose yields span a wide range of masses and metallicities (see Table 1), although still with very significant nitrogen production by stars with $m > 4\ \mathrm{M}_\odot$. Later, armed with new stellar prescriptions, MAR calculated stellar yields for stars of masses between 1 and 5 $\mathrm{M}_\odot$. In her work, she suggested that stars with masses greater than 5 $\mathrm{M}_\odot$ end their lives as SN-II, thus only stars between 3 and 5 $\mathrm{M}_\odot$ contributed to the nitrogen production. The final result was a small excess in ^{12}C and a paucity of ^{14}N.[3]

GAV published new yields for low and intermediate mass stars, with masses up to 8 $\mathrm{M}_\odot$ and a range of metallicities (see Table 1). The main point of their work was the treatment of ^{12}C and ^{14}N, concluding that a great amount of ^{12}C in the ISM was ejected by intermediate stars, leading to ^{14}N yields not as great as VHK, nor as low as MAR, and reproducing well the observational constraints related to the time evolution of the elemental and relative abundances of C, N, and O, throughout the disc and halo.[4]

Table 1. Characteristics of the low and intermediate mass stellar yields used in this work.

Set name	Z	Mass range ($\mathrm{M}_\odot$)	Yield format	Solar abundances
VHK	0.001	0.8–8	$q_i(m)$	AG89
	0.004			
	0.008			
	0.020			
MAR	0.004	0.8–5	$mq_i(m)$	GA91
	0.008			
	0.020			
GAV	0.0126	0.8–8	$q_i(m)$ and $m_{\mathrm{eje},\,i}(m)$	GS98
	0.0159			
	0.0200			
	0.0250			
	0.0317			
KAR	0.0001	1–6	$q_i(m)$ and $m_{\mathrm{eje},\,i}(m)$	AG89
	0.004			
	0.008			
	0.020			

Notes. AG89: Anders & Grevesse (1989); GA91: Grevesse & Anders (1991); GS98: Grevesse & Sauval (1998).

We use the stellar yields from VHK, MAR, GAV, and KAR for low and intermediate mass stars. Other excellent, more recent sets, such as Cristallo et al. (2011) or Lagarde et al. (2011) are less useful for our purpose here in that they either do not yet provide the full mass spectrum (the former compilation) or the CNO elements needed for our current work (the latter compilation).

From these sets, VHK and MAR give their results as a fraction of stellar mass, $q_i(m)$, and as mass, $mq_i(m)$, respectively, while GAV and KAR give both, (net) stellar yields, $mq_i(m)$, and (total) ejected masses $m_{\mathrm{eje},\,i}(m)$ (see equation 1). The relationship between both quantities depends on the initial abundances $X_{i,\,0}$, usually assumed to be scaled to the solar ones for each value of the total abundance Z

$$X_{i,0} = X_{i,\odot}\,\frac{Z}{Z_\odot}, \tag{3}$$

while H and He abundances are take to be linear functions with Z:

$$\mathrm{H} = \mathrm{H_p} - \frac{\mathrm{H_p} - \mathrm{H_\odot}}{\mathrm{Z_\odot}}\, Z, \tag{4}$$

$$\mathrm{He} = \mathrm{He_p} + \frac{\mathrm{He_\odot} - \mathrm{He_p}}{\mathrm{Z_\odot}}\, Z. \tag{5}$$

Thus, the initial abundances of each element, $X_{i,\,0}$ depend on the total abundance Z and also on the assumed solar values, $X_{i,\,\odot}$ and for the case of the H and He on the primordial values, $\mathrm{H_p}$ and $\mathrm{He_p}$, (Coc et al. 2012; Jimenez et al. 2003) as well. Solar abundances used are different for each set, as specified in Table 1; the range of masses and metallicities are also listed there. We have interpolated the tables given by these authors to obtain the ejected masses for the same seven metallicities: $Z = 0.0$, 0.0001, 0.0004, 0.004, 0.008, 0.02, and 0.05. We have also normalized the four sets, calculating comparable stellar yields $q_i(m)$, for each. Table 2 gives these results

[3] The impact of AGB yield selection, including Renzini & Voli (1981), VHK, and MAR yields, as applied to CEM models of the Milky Way halo was explored by Gibson & Mould (1997).

[4] The evolution N/O and its relation to O/H is beyond the scope of this work, but forms the basis of studies such as Gavilán et al. (2006) and Mollá et al. (2006).

Table 2. Stellar yields $q_i(m)$ for our *lim* sets. This is an example of the results for VHK and $Z = 0.02$. The complete tables 2a to 2d for VHK, MAR, GAV, and KAR for the seven metallicities, are provided in the electronic edition. We give for each stellar yield set, the metallicity Z, and stellar mass, m, the stellar yields, $q_i(m)$, for elements as labelled, the remnant mass, $m_{\rm rem}$, and, in the last two columns, the secondary contributions of $^{13}C_S$ and $^{14}N_S$.

Z	m $M_\odot$	H	D	^{3}He	^{4}He	^{12}C	^{13}C	N	O	$m_{\rm rem}$ $M_\odot$	$^{13}C_S$	$^{14}N_S$
0.02	3.00	−3.86E−02	−3.81E−05	−2.30E−05	3.28E−02	5.25E−03	6.40E−05	1.65E−03	4.11E−04	0.62	4.15E−06	1.37E−04
0.02	3.50	−3.84E−02	−3.83E−05	−2.31E−05	3.26E−02	5.01E−03	6.66E−05	1.72E−03	3.16E−04	0.71	3.47E−06	1.15E−04
0.02	4.00	−3.75E−02	−3.85E−05	−2.33E−05	3.11E−02	4.77E−03	6.83E−05	1.78E−03	1.98E−04	0.79	2.79E−06	9.47E−05
0.02	4.50	−3.78E−02	−3.89E−05	−2.35E−05	3.18E−02	2.08E−03	1.08E−04	4.82E−03	1.58E−04	0.85	2.82E−06	9.89E−05
0.02	5.00	−3.85E−02	−3.92E−05	−2.37E−05	3.09E−02	−5.94E−04	1.40E−04	7.24E−03	1.42E−04	0.92	2.71E−06	1.04E−04

for the suite of low and intermediate mass star yields employed here.

The inferred solar abundances have (in large part) reduced from AG89 to the most recent values, such as those from Asplund et al. (2009). Since the stellar evolution models employed here were constructed with the classic solar abundances, the yields must be used assuming that stars have those abundances. However, when analysing our results for the solar region, we will use the most recent values (Asplund et al. 2009).

To compare the different sets, we plot in Fig. 1 the stellar yields, q_i, as a function of the stellar mass, for He, ^{12}C, ^{13}C, N, and O. Although all sets show a broad similarity for each element, differences arises when we observe their behaviour in detail. As a generic result, MAR differs the most from the others, with a larger production for all elements and also a stronger dependence on Z, while VHK shows the smallest values. This is clear in the He panels, as for ^{12}C, for which all sets show a maximum around 4 $M_\odot$ and where MAR produces double the quantity of ^{12}C than KAR or GAV. For ^{13}C, one can see a strong mass-dependence, with an abrupt increase for stellar masses only near 3 $M_\odot$.

The stellar yield of N for these low and intermediate mass stars is very important since most of N proceeds from this stellar range and because a large contribution of the produced N is primary (NP): that is, independent of the original metallicity of the star. This NP is created in the HBB process, which needs a minimum core mass to initiate, as it occurs with the primary component of the ^{13}C, as well. N appears for stellar masses around 4 $M_\odot$ and when it appears, the ^{12}C consequently decreases. The behaviour is similar for all sets, except for MAR, which does not show, unlike the others, the increase at the highest mass. For O, the stellar yield is essentially negative (and very low in an absolute sense) for the entire mass range; only MAR shows positive values.[5] This negative yield will have consequences when the total integrated yield for oxygen is used, since the number of stars in this mass range is very high, compared with the number of the massive ones which produce the bulk of the oxygen.

The contribution of the primary N in galaxies leads to the classical relationship between N/O and O/H, in which a clear correlation for high metallicity/bright massive galaxies exists, but essentially none for low metallicity/low mass systems. Both contributions are separately given, or easily obtained, for GAV and MAR stellar yields, but for VHK and KAR it was necessary to calculate the primary contribution by the method described in Gavilán et al. (2006). The ratio NP/N is shown in Fig. 2 for the four sets of low and intermediate stars used in this work. Obviously, the ratio NP/N is unity for $Z = 0$ and decreases as NS (secondary nitrogen) increases with Z.

2.1.2 Massive star stellar yields

The generation of massive star yields in the literature show the deployment of a range of evolutionary codes with different assumptions regarding stellar microphysics, including opacities and nuclear reaction rates, and/or macrophysics, such as mixing or mass-loss prescriptions. The NuGRID collaboration (Pignatari et al. 2013) has been established to rectify this heterogeneous situation, by employing an entirely homogeneous micro- and macrophysics approach across the full mass and metallicity spectrum (from low- to high-mass stars). However, at the time of pursuing this work, the only

[5] See also Pignatari et al. (2013) for further recent evidence for modest positive O stellar yields in this mass range.

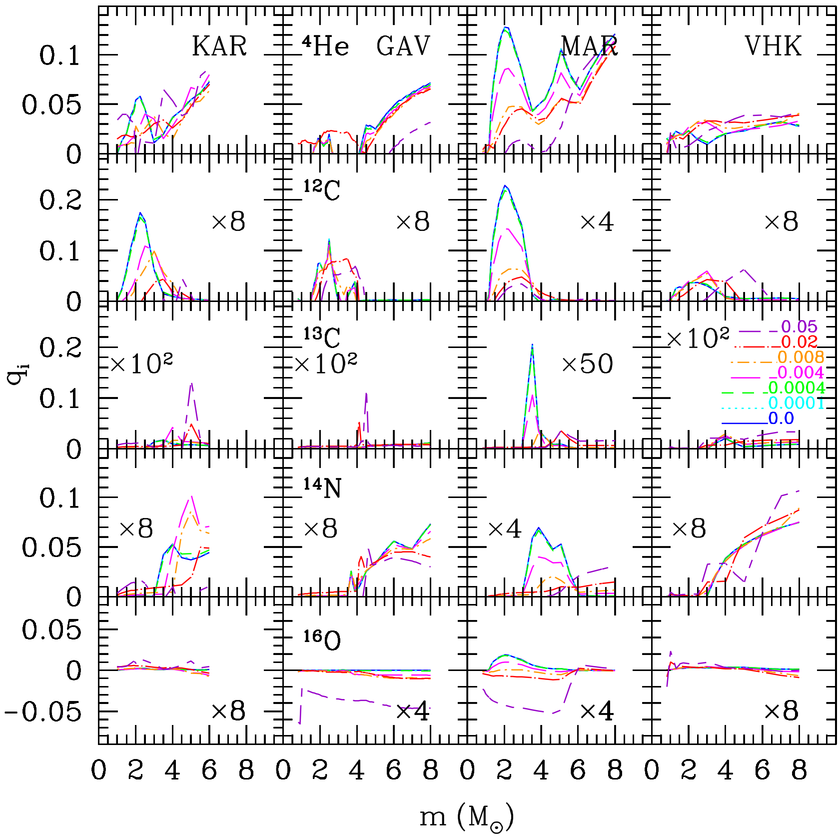

Figure 1. Stellar yields for low and intermediate star. Each row shows an element, He, ^{12}C, ^{13}C, N, and O, from top to bottom, and each column refers to a different yield set as labelled. The number in each panel is the factor used to multiply the yields to plot all of them on a similar *y*-axis scale. In each panel, the coloured lines represent different metallicities as labelled in the ^{13}C panel from VHK.

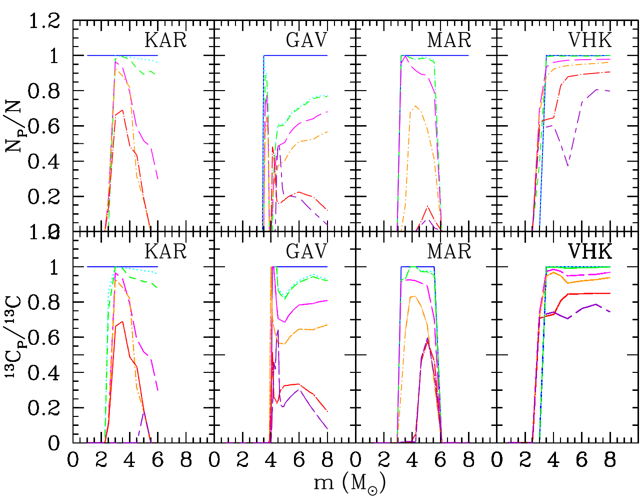

Figure 2. Ratio of primary to total stellar yield for ^{13}C and N. Top panels: N_P/N; Bottom panels: $^{13}C_P/^{13}C$, for *lim* sets by KAR, GAV, MAR, and VHK for different metallicities, as labelled in Fig. 1.

yields available publicly are for masses in the range [1.5–5] M$_\odot$ and [15–60] M$_\odot$ for $Z = 0.02$ (for $Z = 0.01$, the massive star range reduces to [15–25] M$_\odot$), without including the super-AGB phase and the SN-Ia stellar yields. Therefore, while the release of this full grid is eagerly anticipated, it is premature to adopt it for these CEMs.

Other well-known stellar yields are those that include a treatment of stellar rotation, the internal mixing and structural changes resulting from which can lead to appreciable changes in the yields of certain elements, in particular nitrogen (Meynet & Maeder 2000, 2002a,b; Chiappini et al. 2006; Hirschi 2007). A rich literature now exists which examines the role of this stellar rotation on stellar nucleosynthesis, although most of them (Ekström et al. 2008; Meynet et al. 2010; Chatzopoulos & Wheeler 2012; Yoon, Dierks & Langer 2012) have emphasized the impact on very low metallicity or Population III models. The lack of an available, fully self-consistent, grid of models spanning a range of mass and metallicity (up to solar) has somewhat restricted their application for chemical evolution studies. The precise treatment of rotational mixing, with velocities varying from 60 to 800 km^{-1} depending upon the authors and codes involved, remains a matter of debate. From a chemical evolution modelling perspective, the adoption of a given rotation velocity (and its mass and metallicity dependence) implies an additional free parameter, increasing the yield options dramatically.[6] Whilst acknowledging the importance of this issue, we feel it premature

[6] Besides that, it is not entirely sure to what degree, or *if*, this rotation is necessary for reproducing observations. For example, Takahashi, Umeda & Yoshida (2014) have realized rotating and non-rotating models for $Z = 0$ for stellar masses between 12 and 140 M$_\odot$. Comparing these models with the three most Fe-deficient stars in the Galaxy, they find that abundances for one of them are well-reproduced by 50–80 M$_\odot$ non-rotating models, the second one is equally well-fitted with non-rotating or rotating 15–40 M$_\odot$ models, and only one of them might require rotating 30–40 M$_\odot$ models.

Table 3. Characteristics of the *mas* sets used in this work.

Set name	Z	Mass range ($M_\odot$)	Mass-loss	Solar abundances
WOW	0.000	13–40	N	AG89
	2×10^{-6}			
	2×10^{-4}			
	0.002			
	0.02			
PCB	0.0004	11–120	Y	AG89
	0.004			
	0.008			
	0.020			
	0.050			
CLI	0.0000	13–35	N	AG89
	10^{-6}			
	10^{-4}			
	0.001			
	0.020			
KOB	0.000	13–40	Y	AG89
	0.001			
	0.004			
	0.020			
HEG	0.000	10–100	Y	LO03
	0.020	12–120		
LIM	0.000	13–80	Y	AG89
	0.020	11–120		

Notes. AG89: Anders & Grevesse (1989); LO03: Lodders (2003).

to proceed with a detailed comparison of the rotationally mixed yields, until a fully self-consistent grid is available and calibrated unequivocally with empirical constraints.

Thus, we use the extant compilations in the literature, including the sets from WOW, PCB, CLI, HEG, KOB, and LIM. In all cases, authors give their results as total ejected masses and most use solar abundances from Anders & Grevesse (1989), except HEG who use Lodders (2003). This is given in column 5 of Table 3, where characteristics of the yields for each set are shown: the metallicities, the stellar mass range, and the inclusion or not of mass-loss.

As noted in Table 3, yields from WOW and CLI do not take into account pre-SN stellar winds and their corresponding mass-loss, a fact particularly important for the most massive stars ($m \geq 30\,M_\odot$), and give yields for an upper mass limited to 40 $M_\odot$. To extrapolate these yields up to 100 $M_\odot$ is problematic, since mass-loss is known to be substantial for these most massive stars. Extrapolation without the inclusion of mass-loss would result in an integrated yield significantly higher than it should be. KOB, PCB, HEG, and LIM take into account a treatment of mass-loss for these massive stars. In the three last sets, yields are provided up to 100–120 $M_\odot$, while KOB gives their results up 40 $M_\odot$. Therefore, we give in Table 4 the stellar yields up to 40 $M_\odot$ for WOW, CLI, and KOB, and up to 100 $M_\odot$ only for PCB, HEG, and LIM. Graphically, we do the same in Figs 3 and 4, in three panels (or columns of panels) at the left and at the right, respectively

The stellar yields for these sets are given in Table 4. We compare, for the same elements as in Fig. 1, the different sets of yields of massive stars in Fig. 3. There, we show the results for each element in a row, for each massive star yield set in a different column, as labelled at the top of the figure. As a generic result, we see a very different behaviour amongst the sets which are calculated without taking into account the existence of mass-loss by stellar winds before the explosion of supernova (e.g. those of WOW and CLI), and those which do include these stellar winds (e.g. those of PCB, HEG, and LIM). Curiously, KOB is more similar to the first ones although formally this set forms part of the latter. The first sets are in the left-most columns, while the other four are in the right-most panels. The ones on the left show a weaker dependence on Z than the ones on the right, which is to be expected, as the mass-loss is assumed to be dependent upon metallicity. In Fig. 3, we plot the yield of all elements multiplied by a factor as labelled in the WOW panel, in order to compare all of them on a similar scale. In all cases, H is negative with values in the range [−0.1,−0.5] depending on the stellar mass, on the metallicity, and on the authors. In LIM there is a strong variation around 30 $M_\odot$, and it becomes positive for the highest abundance. The behaviour for HEG shows quite abrupt changes with mass due to the $Z = 0$ set.

Since He is produced directly from H, its behaviour is complementary to that of H, increasing when H decreases, although the absolute value is smaller than that, since a certain quantity is necessary to create the other elements. The ejected mass of He and ^{12}C is higher in the case of PCB, HEG, and LIM than those of WOW, CLI, and KOB. When we compare the same mass range we see that for $m \leq 40\,M_\odot$ more He, C, and N is ejected, while O is produced in a smaller quantity when the mass-loss by stellar winds is included.

For the elements beyond O, the yields are shown in Fig. 4 for the six different sets of massive stellar yields. Here, we add the yields for elements Ne, Mg, Si, S, and Ca and represent this α-yield as a

Table 4. Stellar yields $q_i(m)$ from different massive stars mas sets. The values for WOW and $Z = 0.02$ are given here as an example. The complete set of tables for WOW, PCB, CLI, KOB, HEG, and LIM, for seven metallicities (Z = 0, 0.0001, 0.0004, 0.004, 0.008, 0.02, and 0.05) are provided in the electronic edition.

Z	m $M_\odot$	H	D	^{3}He	^{4}He	^{12}C	^{16}O
0.02	22.00	−0.240E+00	−0.436E−04	−0.701E−06	0.908E−01	0.823E−02	0.100E+00
0.02	25.00	−0.270E+00	−0.440E−04	−0.144E−05	0.925E−01	0.101E−01	0.122E+00
0.02	30.00	−0.309E+00	−0.449E−04	−0.319E−05	0.886E−01	0.686E−02	0.155E+00
0.02	35.00	−0.335E+00	−0.452E−04	−0.472E−05	0.801E−01	0.632E−02	0.158E+00
0.02	40.00	−0.331E+00	−0.415E−04	−0.570E−05	0.867E−01	0.648E−02	0.143E+00

^{20}Ne	^{24}Mg	^{28}Si	^{32}S	^{40}Ca	^{56}Fe	m_{rem}	$^{13}C_S$	$^{14}N_S$
0.319E−02	0.356E−03	0.157E−01	0.723E−02	0.423E−03	0.841E−03	2.02	0.375E−04	0.206E−02
0.158E−01	−0.113E−02	0.121E−01	0.504E−02	0.301E−03	0.821E−03	2.07	0.320E−04	0.216E−02
0.144E−01	0.782E−02	0.100E−01	0.272E−02	0.692E−04	0.787E−03	1.94	0.265E−04	0.244E−02
0.254E−01	0.661E−02	0.271E−02	−0.132E−03	−0.335E−03	0.738E−03	2.03	0.205E−04	0.254E−02
0.310E−01	0.429E−02	0.916E−03	−0.274E−03	−0.308E−03	0.658E−03	5.45	0.161E−04	0.257E−02

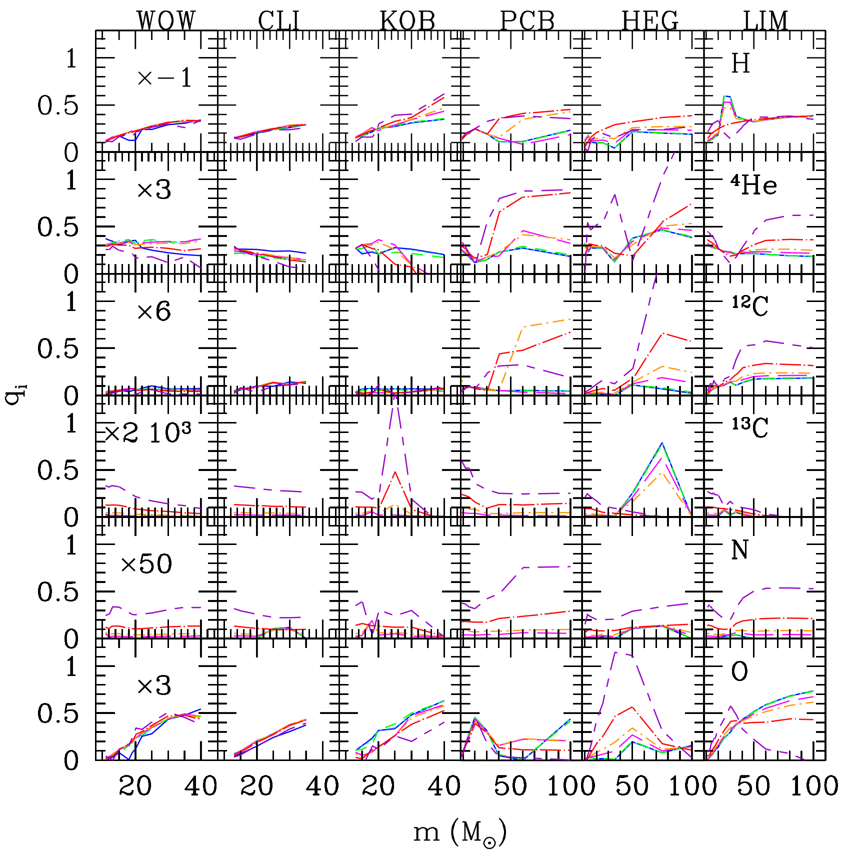

Figure 3. Stellar yield for H, He, ^{12}C, ^{13}C, N and O for massive stars from sets by WOW, CLI, KOB, PCB, HEG, and LIM, for different metallicities coded as in Fig. 1.

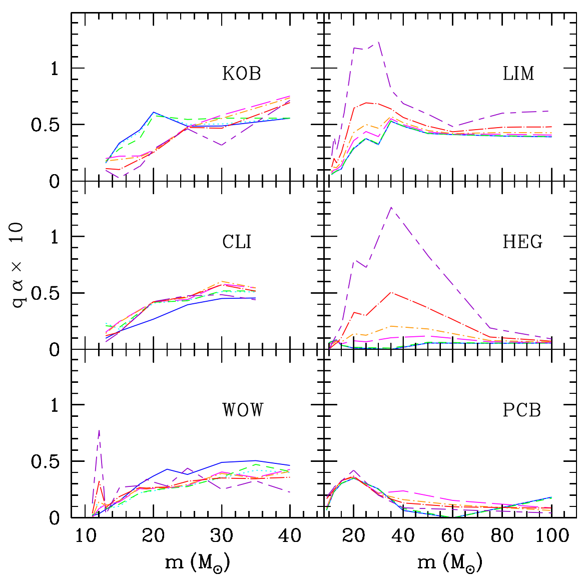

Figure 4. Stellar yield for α-elements $\alpha = ^{20}\mathrm{Ne} + ^{24}\mathrm{Mg} + ^{28}\mathrm{Si} + ^{32}\mathrm{S} + ^{40}\mathrm{Ca}$ for *mas* sets for different metallicities. Lines are coded as in the previous figures.

function of the stellar mass for each yield set. As for O, a different behaviour arises between the yields calculated taking into account the stellar winds (right-hand panels) and those which do not (left-hand panels); the former show a maximum around 20–30 M$_\odot$. KOB shows a behaviour between both, similar to those without mass-loss, but also indicating a slight maximum near 40 M$_\odot$.

2.2 The Initial mass function

We are building upon the Galactic model outlined in MD05, but instead of simply using the FER IMF (as we did in that work), we now employ a range of functional forms for the IMF, as well as the various stellar yield data sets described in Section 2.1. The IMFs adopted are from SAL, MIL, FER, KRO, CHA, and MAS, as shown in Fig. 5, where differences amongst them appear readily. We assumed the IMF to be invariant with time and metallicity.

The functional forms for the adopted IMFs are

$$\phi(m)_{\mathrm{SAL}} = m^{-2.35}, \tag{6}$$

$$\phi(m)_{\mathrm{MIL}} = \mathrm{e}^{\frac{(\log m + 1.02)^2}{20.68^2}}, \tag{7}$$

$$\phi(m)_{\mathrm{FER}} = 10^{-\sqrt{0.73 + \log m(1.92 + 2.07\,\log m)}}/m^{1.52}\,, \tag{8}$$

$$\phi(m)_{\mathrm{KRO}} = \begin{cases} m^{-0.35} & 0.15 \le m/\mathrm{M}_\odot < 0.08 \\ 0.08m^{-1.3} & 0.08 \le m/\mathrm{M}_\odot < 0.50 \\ 0.04m^{-2.3} & 0.50 \le m/\mathrm{M}_\odot < 1 \\ 0.04m^{-2.7} & m/\mathrm{M}_\odot \ge 1 \end{cases} \tag{9}$$

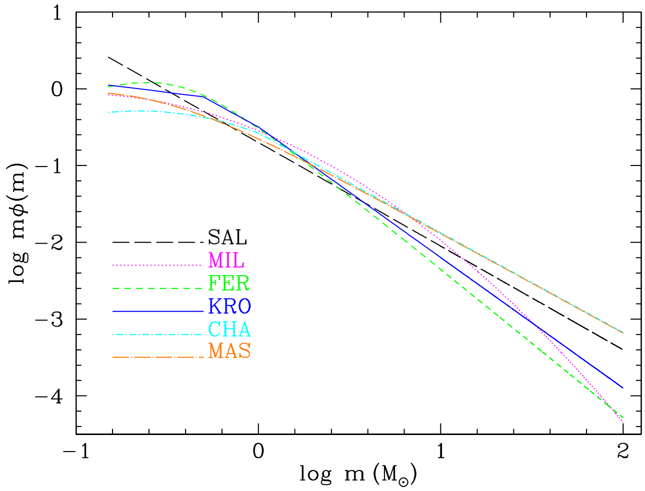

Figure 5. The IMFs used in this work as $\log m\phi(m)$ by SAL, MIL, FER, KRO, CHA, and MAS.

$$\phi(m)_{\rm CHA} = \begin{cases} 0.086 m^{-1} e^{-\frac{(\log m + 0.657)^2}{2\,0.57^2}} & 0.15 \le m/{\rm M}_\odot < 1 \\ 0.043 m^{-2.3} & 1 \le m/{\rm M}_\odot \le 100, \end{cases} \quad (10)$$

$$\phi(m)_{\rm MAS} = AA \left(\frac{m}{m_{\rm char}}\right)^{-\alpha} \left\{1 + \left(\frac{m}{m_{\rm char}}\right)^{1-\alpha}\right\}^{-\beta}, \quad (11)$$

where $m_{\rm char} = 0.2\,{\rm M}_\odot$, (12)

$$G(m) = \left(1 + \left(\frac{m}{m_{\rm char}}\right)^{1-\alpha}\right)^{1-\beta}, \text{ and} \quad (13)$$

$$AA = \frac{(1-\alpha)(1-\beta)}{m_{\rm char}} \frac{1}{G(m_{\rm up}) - G(m_{\rm low})}. \quad (14)$$

As usual, the total mass in stars is normalized to 1 M$_\odot$

$$\int_{m_{\rm low}}^{m_{\rm up}} A\, m\, \phi(m)\, {\rm d}m = 1\,{\rm M}_\odot \quad (15)$$

and in this way, the total number of stars, N_* in a generation is

$$N_* = \int_{m_{\rm low}}^{m_{\rm up}} A\, \phi(m)\, {\rm d}m. \quad (16)$$

Our initial plan was to use the same lower ($m_{\rm low} = 0.15\,{\rm M}_\odot$) and upper ($m_{\rm up} = 100\,{\rm M}_\odot$) mass limits for each CEM; however, as noted previously, some yield compilations are restricted to $\leq$40 M$_\odot$. As such, we have computed the number of stars for each IMF for these two values of $m_{\rm up}$ (see Table 5) and in the next section, models have been computed for each combination of IMF+massive stars with a different $m_{\rm up}$ following the set of massive stars used.

3 CHEMICAL EVOLUTION MODELS

3.1 Summary description

The chemical evolution code used here is that described in MD05 and Mollá (2014), and in Mollá et al. (2015, hereafter MCGD), the latter in which we present a new updated grid of CEMs for spiral, irregular, and low-mass galaxies with some modifications in the input parameters over the ones from MD05.

Table 5. Number of stars for the adopted IMFs for a stellar mass of 10^4 M$_\odot$. We show the normalization constant A, the total number of stars, N_*, the number of stars with mass smaller than 1 M$_\odot$, $N_{\rm low}$, the number of low and intermediate mass stars, with $4\,{\rm M}_\odot \le m \le 8\,{\rm M}_\odot$, $N_{\rm lim}$, the number of massive stars with $m > 8\,{\rm M}_\odot$, which will be SN-II, $N_{\rm SN}$, and the number of stars more massive than 20 M$_\odot$, $N_{\rm mas}$.

IMF	A	N_*	$N_{\rm low}$	$N_{\rm lim}$	$N_{\rm SN}$	$N_{\rm mas}$
			$m_{\rm up} = 40\,{\rm M}_\odot$			
SAL	2090	20 200	19 970	145	83	17
MIL	191	13 387	13 093	214	79	9
FER	22 000	18 924	18 792	98	34	5
KRO	80 830	17 100	16 925	124	51	8
CHA	148 210	11 125	10 780	215	129	26
MAS	13 110	13 133	12 800	206	125	25
			$m_{\rm up} = 100\,{\rm M}_\odot$			
SAL	2000	19 715	19 490	138	86	23
MIL	189	13 329	13 037	212	80	11
FER	21 869	18 837	18 704	98	35	6
KRO	79 458	16 932	16 756	123	54	10
CHA	137 808	10 386	10 055	200	131	36
MAS	12 222	12 319	11 999	192	128	35

We assume a radial distribution of primordial gas in a spherical protohalo falls on to the plane defining the disc.[7] The mass radial distributions are calculated from the prescriptions in Salucci et al. (2007), who give expressions to compute the halo density, virial radius, rotation curve, and final mass of the disc as functions of the virial mass, $M_{\rm vir}$. We have calculated an initial mass distribution with a dynamical mass of $\sim 10^{12}$ M$_\odot$ and a maximum rotation velocity of $V_{\rm rot} = 177\,{\rm km\,s^{-1}}$. The infall rate or collapse time-scale in each radial region is chosen in such a way that the disc ends with a radial profile similar to that observed, by following the prescriptions from Shankar et al. (2006) for the ratio Mdyn/Mdisk, at the end of the evolution for a time of 13.2 Gyr. This method gives as a result, for the chosen virial mass, a radial distribution of the final mass of the disc $M_D(R)$ and also the collapse time-scale radial distribution, $\tau(R)$, necessary to obtain it.

Our formalism for the SFR adopts two stages, first forming molecular clouds from the diffuse gas according to a Schmidt law with $n = 1.5$, and then second, forming stars from cloud–cloud collisions. Once choosing the total mass radial distribution, it is necessary to determine which are the best efficiencies to form molecular clouds and stars for this MWG-like galaxy. This has been performed in MCGD, comparing the time evolution of the region located at $R = 8$ kpc and the radial distributions of gas, stars, and SFR with the present-time data. This comparison allowed us to select and fix the best efficiencies to reproduce the MWG disc data, which are the one used in this work.

For this basic model, we have computed all possible combinations of the six IMFs with the six *mas* sets and the four *lim* yields described in Section 2, resulting in a total of 144 models for the MWG. In order to identify the best combination capable of reproducing the extant observations, we will now compare the results of these models with the observational data given in Appendix A where, furthermore, the

[7] The code is inherently one-dimensional (in r), involving a thin disc and azimuthal symmetry.

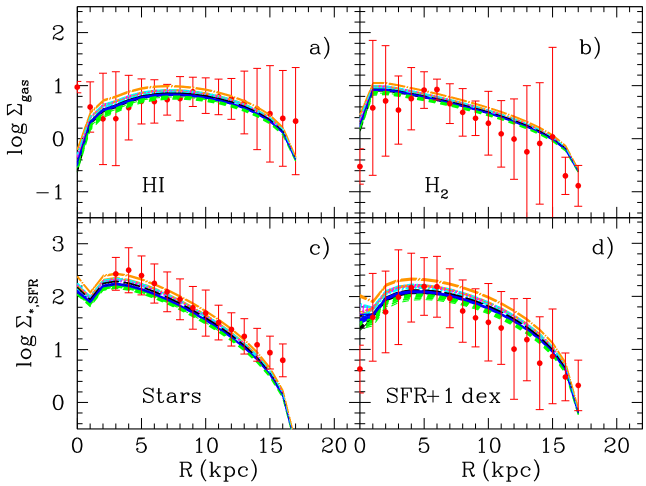

Figure 6. The radial distributions of the MWG disc surface densities for the sets of 144 models compared with the observational data as red dots with error bars: (a) the surface density of diffuse gas, $\Sigma_{\rm HI}$, (b) molecular gas, Σ_{H_2}, (c) stars, Σ_*, in units of $M_\odot$ pc^{-2} for all of them, and (d) SFR, $\Sigma_{\rm SFR}$, in units of $M_\odot$ pc^{-2} Gyr^{-1}. All panels are given in logarithmic scale. Each colour-type of line indicates a different IMF with the same coding as in Fig. 5.

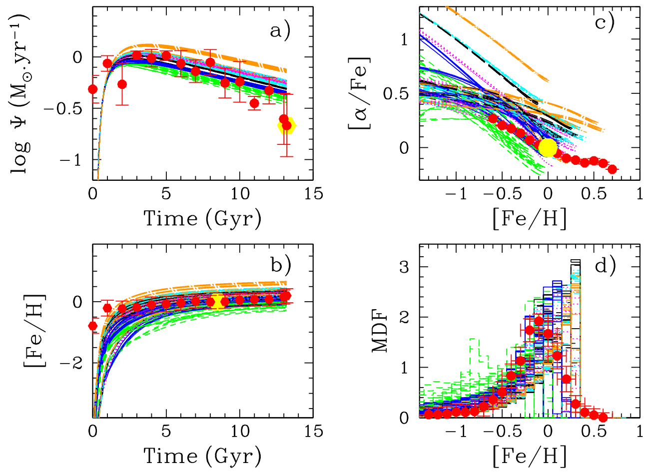

Figure 7. The evolution of the solar neighbourhood for the set of 144 models compared with observational data as red dots with error bars, as obtained in Section A1. The large yellow dot represents the solar values. (a) SFR (in $M_\odot$ yr^{-1}) in logarithmic scale; (b) [Fe/H]; (c) [α/Fe] versus [Fe/H]; (d) The MDF. The coding of the lines is as in Fig. 6.

empirical data has been binned in order map these on to our model bins.

3.2 Results for the Solar Vicinity and the MWG disc

In Fig. 6 we present, for the 144 models, the results concerning the state of the disc or the radial distributions at the present time ($t = 13.2$ Gyr) for gas, stars, and the SFR, compared with the data shown in Table A3. For the SFR, panel (d), we have artificially increased all values (models and data) by 1 dex, in order to plot them in the same scale as used in panel (c). The results show a small dispersion around the data or around the mean values. These good results are the consequence of the infall rate and the SFR efficiencies selected for the model to reproduce the MWG. In all cases the models' dispersions are comparable to, or smaller than, the data uncertainties. These radial distributions are, as expected, only slightly dependent upon the IMF, due to the different rate of ejected/returned gas by (mostly massive) stars when they die.

The evolution of the SFR, metallicity, [α/Fe] as a function of [Fe/H], and the Metallicity Distribution Function (MDF) for the solar region of our 144 models are compared with the observational data given in Tables A1 and A2 in Fig. 7. It is quite evident that, even with the same input parameters and total mass for MWG, the resulting evolution is different for each model. In the case of the SFR, this is due to the IMF used, since the value of the mass locked in stars (1-R) changes with IMF. Thus, the evolution for FER shows the lowest SFR histories while MAS models show the highest, since the returned gas fraction of each stellar generation is the lowest for the FER models. Within each IMF, each combination *mas+lim* also shapes the results somewhat, but in this panel the yields have a smaller role than the IMF. In panel (b), the results are the consequence of the SFR history, and, therefore, again FER is in the lowest part of the model locus while MAS is in the highest. Since Fe is produced mainly by the SN-Ia, the results depend more on IMF than on the stellar yields of massive stars; they do not depend upon the low- and intermediate-mass stars.

In panel (c), we show the classical plot of [α/Fe]–[Fe/H] for the solar region, where [Fe/H] is often taken as a proxy for time. This figure gives the differences in the ejection to the ISM of α-elements, coming from massive stars, and from the Fe ejected mainly by SN-Ia, and also partially due to *mas* yields. Therefore, both IMF and massive stellar yields are playing a role here. It is evident that a 'by eye' inspection of these panels would suggest that the KRO, CHA, MIL, and SAL in our models reproduce better the data. When we use MAS, results fall above the data for all combinations of stellar yields, while our models using FER tend to lie below the observations. This plot also gives an indication concerning the massive star yields + IMF combinations which may be rejected: WOW is only valid when used with FER. In fact, WOW have already noted that their Fe yield is high and recommend it be divided by a factor of 2 in order to best reproduce the data with a CEM. This high Fe yield is compensated for when using FER, since the number of massive stars is small in this IMF compared with the others. In panel (d) it is again evident that the IMF has an important effect on the MDF, with most of FER models at the left and MAS models at the right of the observations. Again our KRO, MIL, and some CHA models seem to fit better the observed MDF.

Finally, we present the resulting radial distributions of C, N, and O for the whole set of 144 models in Fig. 8, compared with the binned data obtained in Section A3. The slope of the radial abundance gradients does not depend, as expected, on the combination *IMF+ stellar yield*. The radial gradient is determined by the ratio between SFR and infall rate, $\Psi(t)/f$, and it is basically independent of the IMF or the stellar yields. This is the reason why the radial gradient is basically the same for the 144 models, since we use the same SFR and infall history for all of them; that said, the absolute abundances change significantly, since, even using the same basic model, the combination *stellar yields+IMF* may change the absolute values of abundances in the disc by a factor of 100 for C, more than a factor of 10 for N, and a factor of 30 for O. Thus, the 144 models results show a dispersion clearly greater than the data and the comparison with data allows us to select the appropriate combination of yields and IMF.

This is the most important result of this section: that it should be possible to select, on the basis of our CEM, which of these

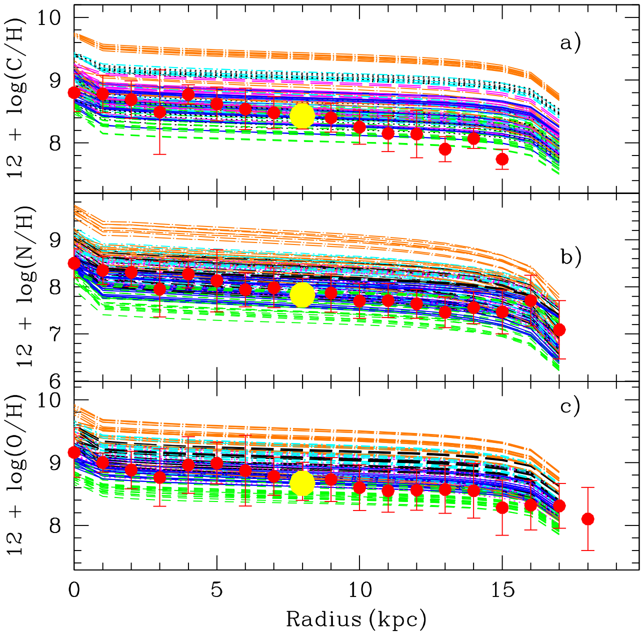

Figure 8. The radial distributions of elemental abundances, as $12 + \log(X/\mathrm{H})$: (a) C, (b) N, and (c) O, in the MWG disc for the sets of 144 models, compared with observational data as red dots with error bars. Coding of the lines is as for Fig. 7.

combinations may be valid in reproducing the empirical data and which of them should be rejected. This is an important point to note as, in order to reproduce a given observation which appears to show a higher or lower metallicity than predicted by a model, a common fall-back option is to invoke some mechanism(s) of mixing, enrichment, or dilution of abundances, to reconcile the discrepancy. As we show here, the alternate suggestion that the correct selection of IMF or/and stellar yields may be an easier way to achieve the desired abundance patterns should not be dismissed.

4 THE SELECTION OF THE BEST MODELS

4.1 The application of a χ^2 technique

The objective of this section is to find the best combination of *IMF + stellar yields* able to reproduce the MWG data amongst the 144 models computed and described in the above section. In order to do this, we use a classical χ^2 technique comparing the model results and the corresponding observational data, such as those used in Figs 6, 7, and 8. In Table 6, we give our χ^2 results; for each model calculated with a combination of *lim* set +*mas* set and IMF, we show the χ^2 obtained from the comparison of our models with the data for all observational sets we use.

As said before and shown in Fig. 6, all models are equally good at fitting the radial distributions of both phases of gas, stars, and the SFR. We confirm this fact with the values of χ^2 for these quantities[8] in Table 6. Basically for all models they fall below the limits corresponding to 80 per cent of confidence level; that is, models fulfill widely these constraints. Therefore, we analyse the fit of our models for the other seven empirical data sets.

We have assumed that each model is represented by a χ^2 distribution, and calculated the corresponding likelihood, P_i, or confidence level, (complement of the significance level α associated[9] to each χ^2). The number of free parameters, $NF = 3$ in all cases, and the number of points for the fitting, $N_{\mathrm{obs},\,i}$, variable for each data set i, give the number of degrees of freedom $k_i = NF - N_{\mathrm{obs},\,i}$. The likelihood is calculated as

$$P_i = 1 - \alpha\left(\chi^2_{k_i} < x\right) = 1 - \int_0^x \chi^2_{ki}\mathrm{d}u$$
$$= 1 - \int_0^x \frac{u^{k_i/2}\mathrm{e}^{-u/2}}{2^{k_i/2}\Gamma(k_i/2)}\mathrm{d}u. \qquad (17)$$

After computing these likelihood values, we see that the SFR and enrichment histories, much like the C, N, and O abundances, may be easily reproduced with some combinations of IMF+ yields, showing low values for χ^2, and high likelihood P_i values. However, the relation [α/Fe]–[Fe/H] and the MDF are more difficult to fit, and thus constrain the selection of models able to reproduce simultaneously all data sets.

In order to choose the best models, we have computed the combined likelihood, P_S

$$P_S = \left(\prod_{i=1, i\neq 2}^{S} P_i\right)^{1/S}, \qquad (18)$$

obtained as the geometrical average of the individual P_i previously calculated for each data set, and S is the number of used data sets. In this expression, we may assume that a good model is the one that simultaneously reproduces all data sets, including the ones pertaining to the present state of the disc, $\Sigma_{\mathrm{H_I}}$, $\Sigma_{\mathrm{H_2}}$, Σ_*, and Σ_{SFR}; in that case, the number of data sets used is $S = 11$. Conversely, we could only use the seven data sets shown in Figs 7 and 8, that is, the observed SFR and enrichment histories, the relation [α/Fe]–[Fe/H], the MDF, and the radial profiles of C/H, N/H, and O/H. Therefore, by maximizing the combined likelihood P_{11} or P_7, we are able to select the best models of our grid. We have computed both values P_{11} and P_7, and then, we have ordered our models by using the combined likelihood P_7 and taken the first eight (which represents ∼5 per cent of the total number of the calculated models), which have values $P_7 > \sim 50$ per cent. The order of models using P_{11} is exactly the same for these models, showing values $P_{11} \gtrsim 65$ per cent. We show these models in Table 7. Only four from our models present values higher than ∼70 per cent for the fit in the seven selected data sets (or >80 per cent in the entire set of observations) and all of them use CLI+KRO combinations. All the other models have $P_7 < 50$ per cent.

These results allow us to constrain the models, reducing the valid ones to only four to eight models, depending on the *goodness* we require. However, we must take into account that this conclusion is mainly due to the MDF, which show values of χ^2 very high compared with most of the models. In fact, besides MAR+HEG+MIL, the 5th in the table, there is only one other model, corresponding to the combination MAR+HEG+SAL, which has a value $\mathrm{P_{MDF}} = 1$.

[8] In all cases, the value at $R = 0$ kpc has not been used in these χ^2 calculations, since the differences between data and models are large in this region, and thus our χ^2 values would be biased towards models with high densities in the inner disc, regardless of the quality of the agreement elsewhere in the disc.

[9] α is the statistical significance, corresponding to a given χ^2, giving the probability of rejecting the null hypothesis, given that it is true, the null hypothesis being that both sets (observations and model results) would represent the same sample.

Table 6. Values of χ^2 obtained from the fitting of models to each one of the data sets defined in Appendix A. The entire table is presented in the electronic version. A portion is shown here for guidance regarding its form and content.

lim	*mas*	IMF	$\chi^2_{\Psi_t}$	$\chi^2_{[\mathrm{Fe/H}]}$	$\chi^2_{[\alpha/\mathrm{Fe}]}$	χ^2_{MDF}	$\chi^2_{\mathrm{H\,I}}$	$\chi^2_{\mathrm{H_2}}$	χ^2_{*}	$\chi^2_{\Psi_R}$	$\chi^2_{\mathrm{C/H}}$	$\chi^2_{\mathrm{N/H}}$	$\chi^2_{\mathrm{O/H}}$
GAV	CLI	SAL	11.768	2.387	70.848	92.836	1.623	5.157	2.517	2.805	51.846	7.614	9.563
GAV	CLI	MIL	17.216	3.894	1.338	112.469	1.803	5.462	1.227	3.669	69.440	13.204	3.302
GAV	CLI	FER	19.522	34.283	43.317	158.274	1.982	5.070	4.553	2.593	23.120	29.962	21.974
GAV	CLI	KRO	14.206	6.894	1.665	50.123	1.666	5.068	3.114	2.743	31.778	5.876	3.925
GAV	CLI	CHA	15.985	6.429	48.694	167.581	1.728	5.411	1.283	3.520	77.556	21.434	13.190
GAV	CLI	MAS	22.255	18.741	154.480	364.015	2.014	5.719	0.690	4.135	119.605	58.290	42.565

Table 7. Confidence levels for the eight best models. For each combination *lim*+ *mas* + IMF, defined in columns 1, 2, and 3, the confidence levels obtained when fitting separately each data set of observations to our models, for columns 4 to 14. Column 15 is the combined likelihood, P_{11}, calculated using all observational sets. Column 16 is P_7, eliminating the disc properties (stars, gas, and SFR radial distributions).

lim	*mas*	IMF	P_{Ψ_t}	$P_{[\mathrm{Fe/H}]}$	$P_{[\alpha/\mathrm{Fe}]}$	P_{MDF}	$P_{\mathrm{H\,I}}$	$P_{\mathrm{H_2}}$	P_{*}	P_{Ψ_R}	$P_{\mathrm{C/H}}$	$P_{\mathrm{N/H}}$	$P_{\mathrm{O/H}}$	P_{11}	P_7
VHK	CLI	KRO	0.997	0.913	1.000	0.502	1.000	1.000	0.994	1.000	0.997	0.999	1.000	0.930	0.894
MAR	CLI	KRO	0.997	0.972	0.995	0.770	1.000	1.000	0.994	1.000	0.799	0.443	1.000	0.885	0.826
GAV	CLI	KRO	0.996	0.881	0.994	0.267	1.000	1.000	0.992	1.000	0.488	1.000	1.000	0.819	0.732
KAR	CLI	KRO	0.998	0.993	1.000	0.108	1.000	1.000	0.994	1.000	0.998	1.000	1.000	0.816	0.727
MAR	HEG	MIL	0.729	0.968	0.129	1.000	1.000	1.000	1.000	1.000	0.383	1.000	1.000	0.737	0.619
MAR	HEG	KRO	0.998	0.729	0.410	0.379	1.000	1.000	0.996	1.000	0.372	0.523	1.000	0.707	0.580
VHK	PCB	FER	0.950	0.697	0.970	0.035	1.000	1.000	0.983	1.000	0.533	1.000	1.000	0.668	0.532
MAR	KOB	KRO	0.996	0.530	0.825	0.069	1.000	1.000	0.993	1.000	0.995	0.265	0.999	0.644	0.501

Table 8. Confidence levels for eight other best models selected without using the MDF.

lim	*mas*	IMF	P_{Ψ_t}	$P_{[\mathrm{Fe/H}]}$	$P_{[\alpha/\mathrm{Fe}]}$	P_{MDF}	$P_{\mathrm{H\,I}}$	$P_{\mathrm{H_2}}$	P_{*}	P_{Ψ_R}	$P_{\mathrm{C/H}}$	$P_{\mathrm{N/H}}$	$P_{\mathrm{O/H}}$	P_{10}	P_6
KAR	KOB	MIL	0.915	0.998	0.998	0.000	1.000	1.000	1.000	1.000	1.000	1.000	1.000	0.991	0.985
KAR	CLI	MIL	0.873	0.939	0.919	0.000	1.000	1.000	1.000	1.000	0.997	1.000	0.999	0.972	0.953
MAR	KOB	MIL	0.908	0.993	1.000	0.000	1.000	1.000	1.000	1.000	0.747	1.000	1.000	0.961	0.936
KAR	PCB	FER	0.958	0.800	0.977	0.009	1.000	1.00	0.982	1.000	0.880	0.996	1.000	0.957	0.932
MAR	CLI	MIL	0.856	0.997	0.999	0.000	1.000	1.000	1.000	1.000	0.465	1.000	1.000	0.912	0.857
KAR	KOB	KRO	0.997	0.661	0.976	0.002	1.000	1.000	0.992	1.000	0.532	0.999	1.000	0.898	0.836
VHK	PCB	FER	0.950	0.697	0.970	0.035	1.000	1.000	0.983	1.000	0.533	1.000	1.000	0.897	0.836
VHK	KOB	KRO	0.994	0.310	0.993	0.016	1.000	1.000	0.993	1.000	1.000	0.999	1.000	0.887	0.821

However, these two models have a $P_{[\alpha/\mathrm{Fe}]} = 0.129$ and 0, respectively, which implies they do not reproduce this relation at all. Actually there is only one model, the first one of the table, with $P_i > 50$ per cent for all columns. If we eliminate the MDF as a constraint for our models and calculate the equivalent P_6 and P_{10}, we find 11 models satisfying this condition for the 10 other columns. Eight of them, shown in Table 8, using MIL or FER as IMF, are able to reproduce the 6 (or 10) remaining data sets within a confidence level P_6 higher than 80 per cent (or ∼90 per cent for P_{10}). In fact, models 1 to 4 in Table 7, showing $P_{11} > 80$ per cent, increase to values $P_{10} > 92$ per cent, when we do not take into account the columns corresponding to the MDF. Therefore, models of this second table would also be valid, considering that many of the literature MDFs of the past decade should have different maxima positions: Casagrande et al. (2011) found this maximum at [Fe/H] ~ -0.05, similarly to Chang, Hou & Fu (2000), Luck & Heiter (2006), Fuhrmann (2008), while Kordopatis et al. (2015) find it near −0.2 dex, more in agreement with Allende Prieto et al. (2004), Nordström et al. (2004), Holmberg, Nordström & Andersen (2007). Although we have used some of these data sets to obtain a bin-averaged MDF, it is likely that the error bars associated with these data are higher than the pure statistical ones included in our χ^2 calculation.

Summarizing, our best models are combinations of CLI–KRO with any *lim* set. It is necessary to note that, given the possible uncertainties in the MDF, perhaps other combinations of stellar yields and IMF, as shown in Table 8, might succeed in reproducing the MWG data, mainly if other hypotheses pertaining to the evolutionary scenario (infall rate or SFR) are assumed.

4.2 Results for the best models

Having selected our best models, we plot their results in the subsequent figures to compare with the observational data. In Fig. 9, we show the evolution with time of SFR, $\Psi(t)$, [Fe/H](t), [α/Fe]–[Fe/H], and the MDF. We have also drawn as an orange dot–dashed line the model MAR+HEG+SAL which does not reproduce the relation [α/Fe]–[Fe/H] as said in the previous section.

Finally, we show in Fig. 10 the elemental abundances of (a) C, (b) N, and (c) O with the same line coding that in the previous Fig. 9. We see in the panel (b) that model using VHK shows the highest N abundances of the four models, just within the limit of the uncertainties, while using MAR, with GAV lying between the two and closest to the date, as also found in GAV. The radial gradient of O abundances obtained with recent data from Henry et al. (2010) and Luck et al. (2011) gives an averaged value of −0.040 dex kpc^{-1}; C data gives a radial gradient of −0.048 dex kpc^{-1}, similar to the one for O. For N we obtain a radial gradient of −0.062 dex kpc^{-1}, slightly steeper than the one for C and O. The four models show

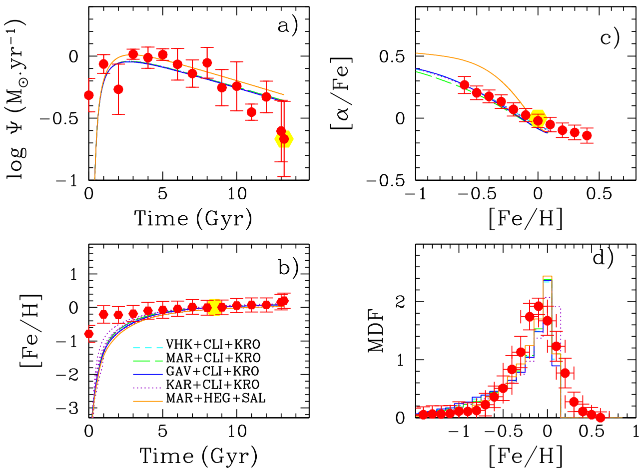

Figure 9. Solar vicinity evolution of the best four models shown in Table 7: (a) $\Psi(t)$, (b) [Fe/H](t), (c) [α/Fe] versus [Fe/H], and (d) MDF. Red and yellow dots have the same meaning as in Fig. 7. The orange dot–dashed line represents the model where $P_{MDF} = 1$ but $P_{[\alpha/Fe]} = 0$.

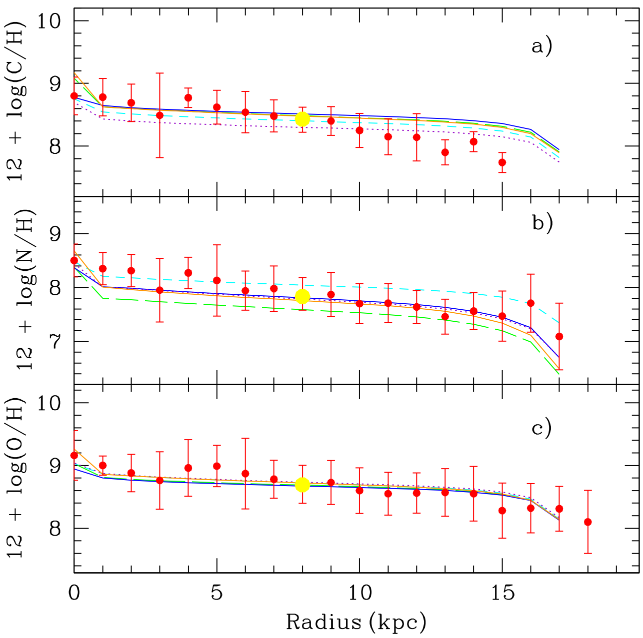

Figure 10. Radial distributions of elemental abundances for the best four models compared with data. The meaning of colours, symbols, and types of lines is the same as in Fig. 9.

radial distributions which seem in fair agreement with the observed radial gradients.

5 CONCLUSIONS

(i) By using our multiphase chemical evolution code, we have calculated 144 models applied to the MWG, with the same basic hypotheses, but different combinations of four low and intermediate mass stellar yield sets, with six massive stellar yield sets, and six IMFs.

(ii) We have analysed the observational data corresponding to the temporal evolution for SFR and iron abundance, the relative abundance [α/Fe] as a function of [Fe/H], and the MDF for the solar region; further, we provided radial distributions of masses and elemental abundances at the present time for the Galactic disc, obtaining binned data sets averaged with different authors' samples.

(iii) Using a classical χ^2 technique, we compared the results of our 144 models with the binned data points from the observational data.

(iv) Assuming that a good model is the one that simultaneously reproduces the observed SFR history, the [α/Fe]–[Fe/H] relation, the MDF, and the radial profiles of C/H, N/H, and O/H, we defined a geometrical averaged likelihood from the product of the individual confidence levels for these seven quantities.

(v) We find that the best 4 of our 144 models are able to reproduce all observational data sets with confidence levels P_7 higher than ∼70 per cent, and use combinations CLI+KRO with any *lim* yields. It is necessary to take into account that, given the possible uncertainties in the MDF, maybe other different combinations of stellar yields and IMF might be equivalently good to reproduce the MWG data, mainly if other assumptions regarding the infall rate or SFR are used.

ACKNOWLEDGEMENTS

This work has been supported by DGICYT grant AYA2010-21887-C04-02. Also, partial support from the Comunidad de Madrid under grant CAM S2009/ESP-1496 (AstroMadrid) is grateful.This work has been financially supported by the grant numbers 2010/18835-3, 2012/22236-3 and 2012/01017-1, from the São Paulo Research Foundation (FAPESP). This work has made use of the computing facilities of the Laboratory of Astroinformatics (IAG/USP, NAT/Unicsul), whose purchase was made possible by the Brazilian agency FAPESP (grant 2009/54006-4) and the INCT-A. M. Mollá thanks the kind hospitality and wonderful welcome of the Jeremiah Horrocks Institute in Preston and of the Instituto de Astronomia, Geofísica e Ciências Atmosféricas in Sao Paulo, where this work was partially done. BKG acknowledges the support of the UK's Science & Technology Facilities Council (ST/F002432/1, ST/H00260X/1, and ST/J001341/1). OC would like to thank H. Monteiro for enlightening discussions. We acknowledge the anonymous referee for very helpful comments.

REFERENCES

Afflerbach A., Churchwell E., Werner M. W., 1997, ApJ, 478, 190
Allende Prieto C., Barklem P. S., Lambert D. L., Cunha K., 2004, A&A, 420, 183
Anders E., Grevesse N., 1989, Geochim. Cosmochim. Acta, 53, 197 (AG89)
Anders F. et al., 2014, A&A, 564, A115
Andrews J. E. et al., 2013, ApJ, 767, 51
Asplund M., Grevesse N., Sauval A. J., Scott P., 2009, ARA&A, 47, 481
Balser D. S., Rood R. T., Bania T. M., Anderson L. D., 2011, ApJ, 738, 27
Bekki K., 2013, ApJ, 779, 9
Bensby T., Feltzing S., Oey M. S., 2014, A&A, 562, A71
Bergemann M. et al., 2014, A&A, 565, A89
Bienaymé O., Soubiran C., Mishenina T. V., Kovtyukh V. V., Siebert A., 2006, A&A, 446, 933
Boeche C. et al., 2013, A&A, 553, A19
Bovy J., Rix H.-W., 2013, ApJ, 779, 115
Burbidge E. M., Burbidge G. R., Fowler W. A., Hoyle F., 1957, Rev. Mod. Phys., 29, 547
Burch B., Cowsik R., 2013, ApJ, 779, 35
Calura F., Recchi S., Matteucci F., Kroupa P., 2010, MNRAS, 406, 1985
Campbell S. W., Lattanzio J. C., 2008, A&A, 490, 769
Carigi L., Peimbert M., 2011, Rev. Mex. Astron. Astrofis., 47, 139
Casagrande L., Schönrich R., Asplund M., Cassisi S., Ramírez I., Meléndez J., Bensby T., Feltzing S., 2011, A&A, 530, A138

Cavichia O., Mollá M., Costa R. D. D., Maciel W. J., 2014, MNRAS, 437, 3688
Chabrier G., 2003, ApJ, 586, L133 (CHA)
Chang R.-X., Hou J.-L., Fu C.-Q., 2000, Chin. Astron. Astrophys., 24, 444
Chatzopoulos E., Wheeler J. C., 2012, ApJ, 748, 42
Chiappini C., Hirschi R., Meynet G., Ekström S., Maeder A., Matteucci F., 2006, A&A, 449, L27
Chieffi A., Limongi M., 2004, ApJ, 608, 405 (CLI)
Chieffi A., Limongi M., 2013, ApJ, 764, 21
Chomiuk L., Povich M. S., 2011, AJ, 142, 197
Cignoni M., Degl'Innocenti S., Prada Moroni P. G., Shore S. N., 2006, A&A, 459, 783
Coc A., Goriely S., Xu Y., Saimpert M., Vangioni E., 2012, ApJ, 744, 158
Conroy C., Dutton A. A., Graves G. J., Mendel J. T., van Dokkum P. G., 2013, ApJ, 776, L26
Cristallo S., Straniero O., Gallino R., Piersanti L., Domínguez I., Lederer M. T., 2009, ApJ, 696, 797
Cristallo S. et al., 2011, ApJS, 197, 17
Daflon S., Cunha K., 2004, ApJ, 617, 1115
Dopcke G., Glover S. C. O., Clark P. C., Klessen R. S., 2013, ApJ, 766, 103
Edvardsson B., Andersen J., Gustafsson B., Lambert D. L., Nissen P. E., Tomkin J., 1993, A&AS, 102, 603
Ekström S., Meynet G., Chiappini C., Hirschi R., Maeder A., 2008, A&A, 489, 685
Esteban C., Peimbert M., Torres-Peimbert S., 1999, A&A, 342, L37
Esteban C., García-Rojas J., Peimbert M., Peimbert A., Ruiz M. T., Rodríguez M., Carigi L., 2005, ApJ, 618, L95
Esteban C., Carigi L., Copetti M. V. F., García-Rojas J., Mesa-Delgado A., Castañeda H. O., Péquignot D., 2013, MNRAS, 433, 382
Fenner Y., Gibson B. K., Gallino R., Lugaro M., 2006, ApJ, 646, 184
Ferreras I., La Barbera F., de la Rosa I. G., Vazdekis A., de Carvalho R. R., Falcón-Barroso J., Ricciardelli E., 2013, MNRAS, 429, L15
Ferrini F., Penco U., Palla F., 1990, A&A, 231, 391 (FER)
Ferrini F., Matteucci F., Pardi C., Penco U., 1992, ApJ, 387, 138
Ferrini F., Mollá M., Pardi M. C., Díaz A. I., 1994, ApJ, 427, 745
Fich M., Silkey M., 1991, ApJ, 366, 107
Flynn C., Holmberg J., Portinari L., Fuchs B., Jahreiß H., 2006, MNRAS, 372, 1149
Forestini M., Charbonnel C., 1997, A&AS, 123, 241
Fröhlich C. et al., 2006, ApJ, 637, 415 (HEG)
Fuhrmann K., 2008, MNRAS, 384, 173
Gavilán M., Buell J. F., Mollá M., 2005, A&A, 432, 861 (GAV)
Gavilán M., Mollá M., Buell J. F., 2006, A&A, 450, 509 (GAV)
Geha M. et al., 2013, ApJ, 771, 29
Gibson B. K., 1997, MNRAS, 290, 471
Gibson B. K., Mould J. R., 1997, ApJ, 482, 98
Gibson B. K., Loewenstein M., Mushotzky F. F., 1997, MNRAS, 290, 623
Gil-Pons P., Doherty C. L., Lau H., Campbell S. W., Suda T., Guilani S., Gutiérrez J., Lattanzio J. C., 2013, A&A, 557, A106
Grevesse N., Anders E., 1991, Solar Interior and Atmosphere. Univ. Arizona Press, Tucson, p. 1227 (GA91)
Grevesse N., Sauval A. J., 1998, Space Sci. Rev., 85, 161
Heger A., Woosley S. E., 2010, ApJ, 724, 341 (HEG)
Henry R. B. C., Kwitter K. B., Jaskot A. E., Balick B., Morrison M. A., Milingo J. B., 2010, ApJ, 724, 748
Hernández-Martínez L., Carigi L., Peña M., Peimbert M., 2011, A&A, 535, A118
Hirschi R., 2007, A&A, 461, 571
Holmberg J., Flynn C., 2004, MNRAS, 352, 440
Holmberg J., Nordström B., Andersen J., 2007, A&A, 475, 519
Iwamoto K., Brachwitz F., Nomoto K., Kishimoto N., Umeda H., Hix W. R., Thielemann F.-K., 1999, ApJS, 125, 439
Jimenez R., Flynn C., Macdonald J., Gibson B. K., 2003, Science, 299, 1552
Kalberla P. M. W., Kerp J., 2009, ARA&A, 47, 27
Karakas A. I., 2010, MNRAS, 403, 1413 (KAR)
Karakas A., Lattanzio J. C., 2007, Publ. Astron. Soc. Aust., 24, 103
Khoperskov A. V., Tyurina N. V., 2003, Astron. Rep., 47, 443
Kobayashi C., Umeda H., Nomoto K., Tominaga N., Ohkubo T., 2006, ApJ, 653, 1145 (KOB)
Kordopatis G. et al., 2015, MNRAS, 447, 3526
Kroupa P., 2001, MNRAS, 322, 231
Kroupa P., 2002, Science, 295, 82 (KRO)
Kuijken K., Gilmore G., 1989, MNRAS, 239, 605
Kuijken K., Gilmore G., 1991, ApJ, 367, L9
Lacey C. G., Fall S. M., 1983, MNRAS, 204, 791
Lagarde N., Charbonnel C., Decressin T., Hagelberg J., 2011, A&A, 536, A28
Läsker R., van den Bosch R. C. E., van de Ven G., Ferreras I., La Barbera F., Vazdekis A., Falcón-Barroso J., 2013, MNRAS, 434, L31
Limongi M., Chieffi A., 2003, ApJ, 592, 404 (CLI)
Limongi M., Chieffi A., 2006, ApJ, 647, 483 (LIM)
Limongi M., Chieffi A., 2012, ApJS, 199, 38 (LIM)
Lodders K., 2003, ApJ, 591, 1220 (LO03)
Luck R. E., Heiter U., 2006, AJ, 131, 3069
Luck R. E., Andrievsky S. M., Kovtyukh V. V., Gieren W., Graczyk D., 2011, AJ, 142, 51
McMillan P. J., 2011, MNRAS, 414, 2446
McWilliam A., Wallerstein G., Mottini M., 2013, ApJ, 778, 149
Marigo P., 2001, A&A, 370, 194 (MAR)
Maschberger T., 2013, MNRAS, 429, 1725 (MAS)
Meynet G., Maeder A., 2000, A&A, 361, 101
Meynet G., Maeder A., 2002a, A&A, 381, L25
Meynet G., Maeder A., 2002b, A&A, 390, 561
Meynet G., Hirschi R., Ekstrom S., Maeder A., Georgy C., Eggenberger P., Chiappini C., 2010, A&A, 521, AA30
Miller G. E., Scalo J. M., 1979, ApJS, 41, 513 (MIL)
Misiriotis A., Xilouris E. M., Papamastorakis J., Boumis P., Goudis C. D., 2006, A&A, 459, 113
Mollá M., 2014, Adv. Astron., 2014, 162949
Mollá M., Díaz A. I., 2005, A&A, 359, 18 (MD05)
Mollá M., Ferrini F., Díaz A. I., 1996, ApJ, 466, 668
Mollá M., Vílchez J. M., Gavilán M., Díaz A. I., 2006, MNRAS, 372, 1069
Mollá M., Cavichia O., Gibson B. K., Díaz A. I., 2015, MNRAS, submitted (MCGD)
Moni Bidin C., Carraro G., Méndez R. A., Smith R., 2012, ApJ, 751, 30
Nakanishi H., Sofue Y., 2003, PASJ, 55, 191
Nakanishi H., Sofue Y., 2006, PASJ, 58, 847
Nordström B. et al., 2004, A&A, 418, 989
Olling R. P., Merrifield M. R., 2001, MNRAS, 326, 164
Pagel B. E. J., 2009, Nucleosynthesis and Chemical Evolution of Galaxies. Cambridge Univ. Press, Cambridge
Peacock M. B., Zepf S. E., Maccarone T. J., Kundu A., Gonzalez A. H., Lehmer B. D., Maraston C., 2014, ApJ, 784, 162
Peek J. E. G., 2009, ApJ, 698, 1429
Peimbert M., 1979, in Burton W. B., ed., Proc. IAU Symp. 84, The Large-scale Characteristics of the Galaxy. Kluwer, Dordrecht, p. 307
Pignatari M. et al., 2013, preprint (arXiv:1307.6961)
Pineda J. L., Langer W. D., Velusamy T., Goldsmith P. F., 2013, A&A, 554, A103
Portinari L., Chiosi C., Bressan A., 1998, A&A, 334, 505 (PCB)
Rana N. C., 1991, ARA&A, 29, 129
Rauscher T., Heger A., Hoffman R. D., Woosley S. E., 2002, ApJ, 576, 323
Reddy B. E., Tomkin J., Lambert D. L., Allende Prieto C., 2003, MNRAS, 340, 304
Renda A. et al., 2004, MNRAS, 354, 575
Renzini A., Voli M., 1981, A&A, 94, 175
Rocha-Pinto H. J., Scalo J., Maciel W. J., Flynn C., 2000, A&A, 358, 869
Romano D., Chiappini C., Matteucci F., Tosi M., 2005, A&A, 430, 491
Romano D., Karakas A. I., Tosi M., Matteucci F., 2010, A&A, 522, A32
Rowell N., 2013, MNRAS, 434, 1549
Rudolph A. L., Fich M., Bell G. R., Norsen T., Simpson J. P., Haas M. R., Erickson E. F., 2006, ApJS, 162, 346
Ruiz-Lapuente P., Blinnikov S., Canal R., Mendez J., Sorokina E., Visco A., Walton N., 2000, MmSAI, 71, 435
Salpeter E. E., 1955, ApJ, 121, 161 (SAL)

Salucci P., Lapi A., Tonini C., Gentile G., Yegorova I., Klein U., 2007, MNRAS, 378, 41
Scalo J., 1998, in Gilmore G., Howell D., eds, ASP Conf. Ser. Vol. 142, The Stellar Initial Mass Function. Astron. Soc. Pac., San Francisco, p. 201
Shankar F., Lapi A., Salucci P., De Zotti G., Danese L., 2006, ApJ, 643, 14
Shaver P. A., McGee R. X., Newton L. M., Danks A. C., Pottasch S. R., 1983, MNRAS, 204, 53
Siebert A., Bienaymé O., Soubiran C., 2003, A&A, 399, 531
Siess L., 2010, A&A, 512, A10
Smith R. J., Lucey J. R., 2013, MNRAS, 434, 1964
Sofue Y., 2013, PASJ, 65, 118
Stancliffe R. J., Jeffery C. S., 2007, MNRAS, 375, 1280
Takahashi K., Umeda H., Yoshida T., 2014, ApJ, 794, 40
Talbot R. J., Jr, 1980, ApJ, 235, 821
Tinsley B. M., 1980, Fundam. Cosm. Phys., 5, 287
Twarog B. A., 1980, ApJ, 242, 242
Urquhart J. S., Figura C. C., Moore T. J. T., Hoare M. G., Lumsden S. L., Mottram J. C., Thompson M. A., Oudmaijer R. D., 2014, MNRAS, 437, 1791
Vallenari A., Bertelli G., Schmidtobreick L., 2000, A&A, 361, 73
van den Hoek L. B., Groenewegen M. A. T., 1997, A&AS, 123, 305 (VHK)
Ventura P., D'Antona F., 2005, A&A, 439, 1075
Ventura P., D'Antona F., 2009, A&A, 499, 835
Vilchez J. M., Esteban C., 1996, MNRAS, 280, 720
Vincenzo F., Matteucci F., Belfiore F., Maiolino R., 2015, MNRAS, preprint (arXiv:1503.08300)
Weber M., de Boer W., 2010, A&A, 509, A25
Weidner C., Kroupa P., Pflamm-Altenburg J., Vazdekis A., 2013, MNRAS, 436, 3309
Williams J. P., McKee C. F., 1997, ApJ, 476, 166
Wolfire M. G., McKee C. F., Hollenbach D., Tielens A. G. G. M., 2003, ApJ, 587, 278
Woosle S. E., Weaver T. A., 1986, ARA&A, 24, 205
Woosley S. E., Weaver T. A., 1995, ApJS, 101, 181 (WOW)
Yoon S.-C., Dierks A., Langer N., 2012, A&A, 542, A113
Zhang L., Rix H.-W., van de Ven G., Bovy J., Liu C., Zhao G., 2013, ApJ, 772, 108

SUPPORTING INFORMATION

Additional supporting information may be found in the online version of this article:

Table 2. Stellar yields $q_i(m)$ for our *lim* sets.
Table 4. Stellar yields $q_i(m)$ from different massive stars mas sets.
Table 6. Values of χ^2 obtained from the fitting of models to each one of the data sets defined in Appendix A.
(http://mnras.oxfordjournals.org/lookup/suppl/doi:10.1093/mnras/stv1102/-/DC1).

Please note: Oxford University Press is not responsible for the content or functionality of any supporting materials supplied by the authors. Any queries (other than missing material) should be directed to the corresponding author for the paper.

APPENDIX A: OBSERVATIONAL DATA

The observational data against which our CEMs are compared are now outlined. These include the solar neighbourhood's temporal evolution, in addition to the present state of the disc, including the radial distributions of surface densities for stars, gas, and SFR, and elemental abundances of C, N, and O. Other data, such as [X/Fe], are usually represented as a function of [O/H] or [Fe/H], with the latter typically being employed as a proxy for time. Thus, we have also used the [α/Fe]–[Fe/H] data of the solar vicinity to compare with our models.

Table A1. Binned SFR and metallicity evolution for the solar vicinity.

Time (Gyr)	log Ψ ($M_\odot$ yr^{-1})	$\Delta(\log\Psi)$	[Fe/H]	Δ([Fe/H])
0	−0.3143	0.1667	−0.788	0.25
1	−0.0631	0.0935	−0.208	0.26
2	−0.2668	0.2510	−0.225	0.25
3	0.0165	0.0507	−0.184	0.24
4	−0.0118	0.1055	−0.097	0.25
5	0.0127	0.0577	−0.073	0.25
6	−0.0651	0.1568	−0.040	0.23
7	−0.1400	0.1372	0.017	0.22
8	−0.0530	0.1534	−0.007	0.22
9	−0.2535	0.1797	0.005	0.22
10	−0.2420	0.2441	0.056	0.21
11	−0.4513	0.0809	0.074	0.21
12	−0.3280	0.1581	0.077	0.21
13	−0.6039	0.3078	0.160	0.23
13.2	−0.6676	0.3759	0.200	0.23

A1 The solar vicinity

For the solar vicinities of our CEMs, we compare with extant observations pertaining to the time evolution of the SFR and the age–metallicity relation. The SFR evolution is taken from Twarog (1980) and Rocha-Pinto et al. (2000). In both cases, the data show a maximum around 8–10 Gyr ago, that is, the onset of the SFR occurred at a time 3–5 Gyr after $t = 0$, in agreement with more recent works of Cignoni et al. (2006) and Rowell (2013). These data are binned in 1 Gyr time-steps for the analysis which follows. The results, given in Table A1, have then been normalized to the most recent values of the SFR in the solar region, corresponding to the final point at 13.2 Gyr. The value for the present-day SFR for the entire MWG is estimated to be in the range [0.8-13] $M_\odot$ yr^{-1} (Rana 1991). Misiriotis et al. (2006) give a value of 2.7 $M_\odot$ yr^{-1}, while Chomiuk & Povich (2011) find 1.9 $M_\odot$ yr^{-1}. Taking into account the ratio of areas of the MWG disc within the optical radius and that of the solar region, we obtain a value of $\Psi_\odot \sim 0.266\, M_\odot$ yr^{-1} for the region located at a galactocentric distance $R = 8$ kpc, in excellent agreement with the used value in Calura et al. (2010). This value is the large yellow dot shown in Fig. A1a). In this figure, we see the time evolution of the SFR once normalized to recover this value $\Psi_\odot \sim 0.266$ at 13.2 Gyr. The values of Ψ are given in Table A1.

In panel (b) of Fig. A1, we show the age–metallicity relation obtained with data from the literature as labelled, binned for each Gyr, as in panel (a). Data from recent surveys such as RAVE (Boeche et al. 2013) or APOGEE (Anders et al. 2014) fall in the same region of the plane in panel (b) when only the solar region[10] data are selected. Our binned results are shown in Table A1. They have been normalized to obtain a value [Fe/H] = +0 in $R = 8$ kpc at a time $t = 8.5$ Gyr, when the Sun was born, implying a shift of +0.1 dex compared with the data of Fig. A1b). In both cases, we have added to the dispersion obtained from the binning process, a systematic error (representing observational uncertainties) of 0.05 and 0.10 dex in columns 3 and 5, respectively. In panel (c), we show the values of the α-element abundances compared with those of iron, with data taken from Casagrande et al. (2011). From the latter, we have selected those stars located between 7.5 and 9.5 kpc that lie within 0.5 kpc pf the

[10] The solar region is defined as a 1 kpc annulus centred on a galactocentric radius of 8 kpc, with a thickness of 200–500 pc.

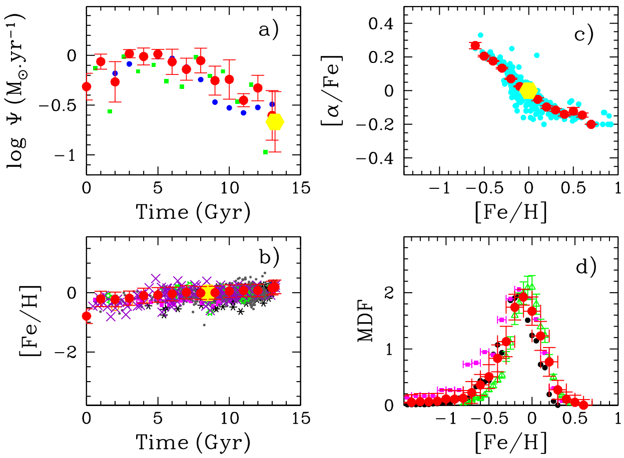

Figure A1. Solar neighbourhood data: (a) Star formation history $\Psi(t)$ with data from Twarog (1980) and Rocha-Pinto et al. (2000) as blue and green dots, respectively; and (b) the age–metallicity relation [Fe/H](t) with data from Twarog (1980), Edvardsson et al. (1993), Rocha-Pinto et al. (2000), Reddy et al. (2003), Casagrande et al. (2011), Bensby, Feltzing & Oey (2014) and Bergemann et al. (2014) as orange open dots, black asterisks, blue full triangles, magenta full squares, grey small dots, green stars, and purple crosses, respectively. The large yellow dots are the solar neighbourhood SFR at the present time in (a) and the solar neighbourhood metallicity at the time when the Sun formed, 4.5 Gyr ago, in (b). (c) [α/Fe] as a function of [Fe/H] from Casagrande et al. (2011, cyan dots). The large yellow dot represents the solar abundances at coordinates (0,0). (d) The MDF with data from Chang et al. (2000), Casagrande et al. (2011) and Kordopatis et al. (2015, RAVE survey) as magenta squares, green triangles and black dots, respectively. In all panels the red dots with error bars are the binned results using all the noted data sets.

Table A2. Binned [α/Fe]–[Fe/H] relation and MDF for the solar vicinity.

Fe/H	[α/Fe]	$\Delta_{[\alpha/Fe]}$	MDF	Δ_{MDF}
−1.50			0.039	0.030
−1.40			0.062	0.040
−1.30			0.063	0.042
−1.20			0.013	0.050
−1.10			0.072	0.038
−1.00			0.129	0.050
−0.90			0.127	0.042
−0.80			0.190	0.100
−0.70			0.147	0.030
−0.60	0.268	0.019	0.411	0.088
−0.50	0.205	0.005	0.502	0.013
−0.40	0.176	0.002	0.886	0.123
−0.30	0.134	0.005	1.440	0.169
−0.20	0.071	0.004	1.900	0.065
−0.10	0.025	0.003	1.870	0.077
0.00	−0.021	0.004	1.500	0.141
0.10	−0.051	0.009	0.971	0.172
0.20	−0.097	0.008	0.769	0.154
0.30	−0.115	0.009	0.239	0.057
0.40	−0.140	0.011	0.076	0.017
0.50	−0.122	0.021		
0.60	−0.145	0.012		
0.70	−0.200	0.000		

mid-plane of the disc, for studying the evolution of the solar neighbourhood. These values are binned and shown in Table A2. In panel (d), we show the MDF. Given the similarity of the three data sets, we have binned and normalized the result to unity, and listed them in Table A2.

A2 The MWG disc: surface densities

The radial gas distributions for both molecular and diffuse phases are well known. Since our model calculates separately both components, we also use these observations to fit our models. We use data from the literature, shown in Fig. A2 for diffuse H I and H_2. By binning both sets, we obtain the results given in Table A3 and shown in panels (a) and (b). We see clearly a maximum around 10 kpc for H I while H_2 shows an exponential shape from 4 kpc to the outer disc. It also shows the well known molecular *hole* inside ∼3 kpc.

In panels (c) of the same Fig. A2 we also show the stellar surface density profile, including estimates from different authors as labelled. The most recent estimates for the solar stellar surface density give values between 33 and 64 $M_\odot$ pc^{-2} (Kuijken & Gilmore 1989, 1991; Vallenari, Bertelli & Schmidtobreick 2000; Khoperskov & Tyurina 2003; Siebert, Bienaymé & Soubiran 2003; Holmberg & Flynn 2004; Bienaymé et al. 2006; Flynn et al. 2006; Weber & de Boer 2010; McMillan 2011; Moni Bidin et al. 2012; Bovy & Rix 2013; Burch & Cowsik 2013; Zhang et al. 2013). These values depend on the scalelength for the disc R_d, which is in the range [2.15–4] kpc. We show these data in panel (c) of Fig. A2 with our results after binning (red dots). In panel (d), we show the SFR

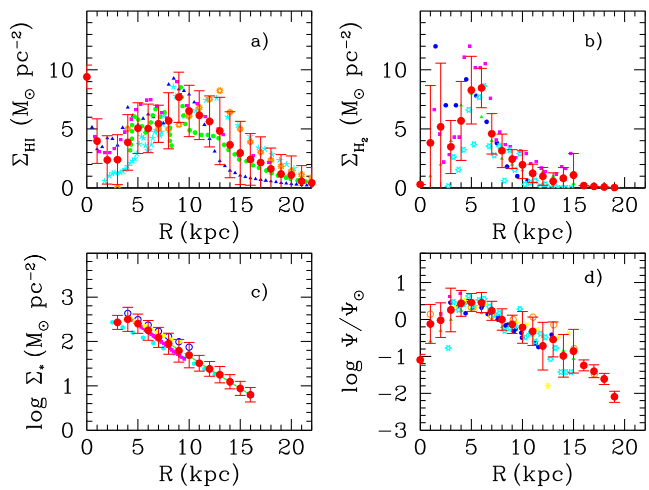

Figure A2. Radial distributions of surface densities in the MWG for: (a) diffuse gas, $\Sigma_{H\,I}$ (in $M_\odot$ pc^{-2} units) with data from Olling & Merrifield (2001), Wolfire et al. (2003), Nakanishi & Sofue (2003), Kalberla & Kerp (2009) and Pineda et al. (2013), as cyan asterisks, orange stars, blue full triangles, green full dots, and magenta full squares, respectively; (b) molecular gas, Σ_{H_2} (in $M_\odot$ pc^{-2} units) with data from Williams & McKee (1997), Nakanishi & Sofue (2006), Pineda et al. (2013) and Urquhart et al. (2014), as green full triangles, blue full dots, magenta full squares, and cyan stars, respectively; (c) Stellar profile Σ_* (in $M_\odot$ pc^{-2} units) with data from Talbot (1980), Rana (1991), Vallenari et al. (2000), Bovy & Rix (2013) and Sofue (2013); (d) the SFR surface density, $\Psi(R)/\Psi_\odot$, normalized to the solar value $\Psi_\odot = 0.266\, M_\odot\, yr^{-1}$, estimated from Misiriotis et al. (2006) and Chomiuk & Povich (2011) in $R = 8$ kpc, with data from Lacey & Fall (1983) and Williams & McKee (1997), as green full triangles and blue full dots, and those taken from Peek (2009) for pulsars, supernovae, and H II regions, shown as yellow stars, orange open dots, and magenta full squares. We have also used those from Urquhart et al. (2014), represented by cyan asterisks. These last two panels are in logarithmic scale. The binned results are the large red dots with error bars in all of them.

Table A3. Radial binned distributions obtained from observational data.

R (kpc)	$\Sigma_{\rm H\,I}$	error	$\Sigma_{\rm H_2}$ $M_\odot$ pc^{-2}	error	log Σ_*	error	log $\Sigma_{\rm SFR}$ $M_\odot$ pc^{-2} Gyr^{-1}	error	C/H	ΔC/H	N/H	ΔN/H	O/H	ΔO/H
0	9.41	1.00	0.30	0.50			−0.370	0.15	(8.66)	(0.30)	8.39	0.31	9.02	0.40
1	3.97	1.88	3.82	4.90			0.603	0.52	(8.64)	(0.30)	(8.24)	(0.30)	(8.86)	0.30
2	2.37	2.04	5.18	5.39			0.706	0.47	(8.55)	(0.30)	(8.20)	(0.30)	(8.74)	0.30
3	2.39	2.12	3.48	2.24	2.43	0.01	0.983	0.59	8.35	0.67	7.84	0.59	8.62	0.45
4	3.86	2.35	5.69	3.35	2.50	0.13	1.163	0.35	8.63	0.15	8.16	0.29	8.82	0.45
5	5.06	2.14	8.28	2.87	2.40	0.07	1.185	0.24	8.48	0.27	8.02	0.66	8.83	0.33
6	5.04	2.06	8.47	1.67	2.25	0.07	1.181	0.27	8.40	0.32	7.83	0.36	8.77	0.56
7	5.44	1.58	4.59	1.72	2.09	0.08	0.963	0.26	8.34	0.25	7.87	0.41	8.69	0.30
8	5.69	2.38	3.15	1.42	1.95	0.09	0.723	0.29	8.28	0.20	7.77	0.30	8.56	0.30
9	7.69	2.13	2.44	0.80	1.79	0.10	0.594	0.25	8.26	0.22	7.76	0.41	8.60	0.35
10	6.52	2.18	1.96	1.18	1.69	0.14	0.510	0.43	8.11	0.27	7.59	0.37	8.45	0.36
11	6.16	2.06	1.24	0.80	1.51	0.03	0.403	0.39	8.01	0.29	7.60	0.36	8.41	0.34
12	5.63	2.17	0.99	0.75	1.38	0.01	0.006	0.65	8.00	0.38	7.53	0.31	8.44	0.32
13	4.83	2.86	0.57	0.71	1.25	0.03	0.183	0.48	7.76	0.20	7.35	0.33	8.44	0.38
14	3.65	2.80	0.82	0.94	1.09	0.01	−0.260	0.57	7.93	0.17	7.45	0.34	8.42	0.43
15	2.96	2.69	1.09	1.84	0.94	0.01	−0.132	0.59	7.60	0.16	7.36	0.47	8.14	0.43
16	2.42	2.19	0.20	0.07	0.80	0.01	−0.520	0.15			7.60	0.54	8.14	0.39
17	2.15	2.17	0.13	0.05			−0.680	0.18			6.98	0.62	8.19	0.35
18	1.61	1.77	0.08	0.03			−0.890	0.15					7.96	0.50
19	1.18	1.66	0.03	0.01			−1.370	0.15						
20	1.10	1.60												

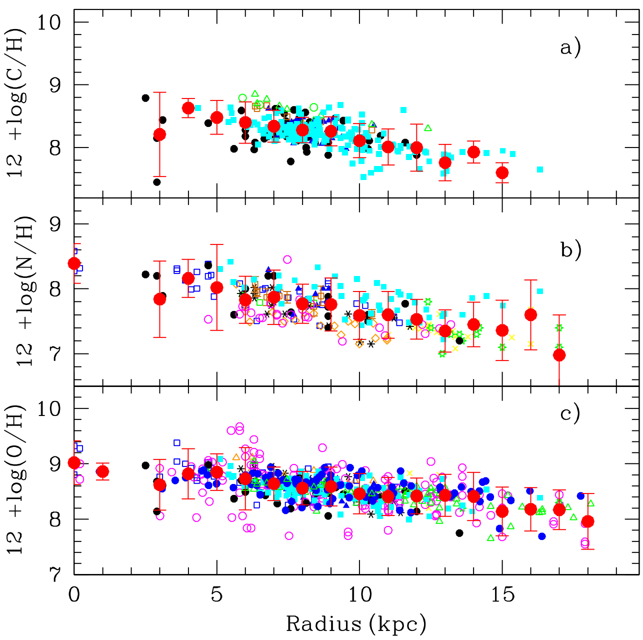

Figure A3. Radial distributions of abundances (as $12 + \log(X/\mathrm{H})$) for (a) C, (b) N, and (c) O. Data are taken from the works noted in Table A4, where the symbol used for each is also given. In all panels the red full dots with error bars are the binned results obtained in this work and given in Table A3.

normalized to the solar value. The binned results for each kpc are also shown as red points, as in panels (a), (b), and (c).

In Table A3, we present the resulting binned-averaged values of diffuse and molecular gas surface densities, and their associated errors, (columns 2 to 5), in $M_\odot$ pc^{-2}, for each radius given in column 1. The stellar surface density profile is given, in logarithmic scale, with its associated error, in columns 6 and 7. In columns 8 and 9, we show the SFR surface density in $M_\odot$ pc^{-2} Gyr^{-1}.

Table A4. List of data sources employed in Fig. A3.

Author	C	N	O	Symbol
Peimbert (1979)	–	X	X	black ∗
Shaver et al. (1983)	–	X	X	orange ◇
Fich & Silkey (1991)	–	X	X	yellow ×
Vilchez & Esteban (1996)	–	X	X	green ⋆
Afflerbach, Churchwell & Werner (1997)	–	X	X	blue ■
Esteban, Peimbert & Torres-Peimbert (1999)	X	X	X	green ○
Reddy et al. (2003)	X	X	X	blue ▲
Daflon & Cunha (2004)	–	X	–	magenta ○
Esteban et al. (2005)	X	X	–	brown □
Gavilán et al. (2006)	X	X	X	black ●
Rudolph et al. (2006)	–	–	X	magenta ○
Henry et al. (2010)	–	–	X	blue ●
Balser et al. (2011)	–	–	X	green △
Luck et al. (2011)	X	X	X	cyan ■
Esteban et al. (2013)	X	–	–	green △

A3 Disc elemental abundances for C, N, and O

C, N, and O abundances are the most important constraints for our models. Since N comes mostly from intermediate mass stars, O from the massive ones, and C from both, a fine-tuning of the stellar yields and IMF is necessary to reproduce simultaneously the three elements. We hope that any of the different combinations of yields from low and intermediate mass stars, with those from massive ones, with different IMFs, would give the right CNO elemental abundances. We show in Fig. A3 the three radial distributions for C, N, and O in panels (a), (b), and (c), respectively. Data from different studies are plotted with different symbols, as listed in Table A4, while the red large dots are again our binned results (as $12 + \log(X/\mathrm{H})$) shown in Table A3.

This paper has been typeset from a TEX/LATEX file prepared by the author.